

Formation and composition of organic aerosols from the uptake of glyoxal on natural mineral dust aerosols: a laboratory study

Francesco Battaglia^{1,a}, Paola Formenti¹, Chiara Giorio², Mathieu Cazaunau³, Edouard Pangui³, Antonin Bergé³, Aline Gratien¹, Diana L. Pereira^{1,b}, Thomas Bertin³, Joel F. de Brito⁴, Manolis N. Romanias⁴, Vincent Michoud¹, Clarissa Baldo^{1,3}, Servanne Chevaillier³, Gael Noyalet³, Philippe Decorse⁵, Bénédicte Picquet-Varrault³, and Jean-François Doussin³

¹ Université Paris Cité and Univ Paris Est Créteil, CNRS, LISA, F-75013 Paris, France

² Yusuf Hamied Department of Chemistry, University of Cambridge, Lensfield Road, Cambridge, CB2 1EW, UK

³ Univ Paris Est Créteil and Université Paris Cité, CNRS, LISA, F-94010 Créteil, France

⁴ IMT Nord Europe, Institut Mines-Télécom, Université de Lille, Centre for Energy and Environment, 59000, Lille, France

⁵ Université Paris Cité, CNRS, Itodys, F-75013 Paris, France

^a now at Dipartimento di Scienze Chimiche, Università degli Studi di Padova, Padova, Italy

^b now at Institute for Atmospheric and Earth System Research, University of Helsinki, Finland

For submission to Atmos. Chem. Phys.

Corresponding author: P. Formenti (paola.formenti@lisa.ipsl.fr)

Abstract

The uptake of glyoxal on realistic submicron mineral dust aerosol particles from a natural soil (Gobi Desert) is investigated during experiments in a large simulation chamber, under variable experimental conditions of relative humidity (RH), irradiation, and ozone concentrations. The uptake of glyoxal on the dust particles starts as soon as the glyoxal is injected into the chamber. At 80% RH, the measured uptake coefficient of glyoxal on mineral dust is $\gamma = (9 \pm 5) \times 10^{-3}$. The totality of the mass of reacting glyoxal is transformed into organic matter on the surface of the dust particles. The uptake of glyoxal is accompanied by the appearance of marker peaks in the organic mass spectra and a persistent growth in the volume concentration of the dust particles. While the mass of the organic matter on the dust rapidly reverts to values prior to uptake, the organic composition of the dust is modified irreversibly. Glycolic and other organic acids, but also oligomers, are detected on the dust. At 80% RH, compounds ranging from C₄ to C₁₀ are observed as oligomerization products of glyoxal mono- and di-hydrate forms. The study suggests that dust aerosols could play a very substantial role in the formation of organic aerosols at high RH, but also that the

reaction could have potentially important implications for the dust optical and hygroscopic properties, including their pH.

1. Introduction

Mineral dust originates naturally from the wind erosion of arid or semi-arid soils, resulting in the suspension of particles with diameters from fractions to hundreds of microns, which can be transported over thousands of kilometres whilst in the atmosphere (Adebiyi et al., 2023; Mahowald et al., 2014). The total global mass of mineral dust particles emitted annually in the atmosphere is of the order of 4600 Tg yr⁻¹, accounting for approximately 40% of the total annual aerosol emissions (Knippertz and Stuut, 2014; Kok et al., 2021). Major natural source areas of mineral dust are North Africa (~50% of the global annual dust emissions), Asia (~40%), North America, and the Southern Hemisphere (~10%; Kok et al., 2023). Anthropogenic emissions are associated with soil erosion for agriculture, pasture, and deforestation (Tegen and Fung, 1995; Webb and Pierre, 2018), but their contribution to the total annual dust mass loading is uncertain, ranging from 5 to 60% (Chen et al., 2023). Mineral dust significantly impacts the Earth's energy balance by absorbing and scattering radiation in the solar and terrestrial spectra (Di Biagio et al., 2019; Kok et al., 2023) and by influencing the lifetime and optical properties of mixed-phase and ice clouds (e.g., Atkinson et al., 2013; Harrison et al., 2001; Steinke et al., 2016). Current estimates of the effective radiative forcing (sum of direct and indirect) of natural mineral dust are in the range of $-0.07 \pm 0.18 \text{ W m}^{-2}$ (Kok et al., 2023), owing to large uncertainties in the atmospheric mass loading and properties of dust at emission and during transport (Castellanos et al., 2024; Li et al., 2021).

Gas-particle interactions along the dust lifecycle contribute to these uncertainties. Numerous laboratory and field studies show that mineral dust is capable to adsorb various reactive gaseous compounds, which may modify its chemical composition, and in turn to alter optical properties, hygroscopicity and ice nucleation activity but also may affect the oxidative capacity of the atmosphere (Bauer et al., 2007; Chirizzi, 2017; Crowley et al., 2010; Joshi et al., 2017; Liu et al., 2013; Ooki and Uematsu, 2005; Romanias et al., 2012; Seisel et al., 2004; Tang et al., 2017; Turpin and Huntzicker, 1995; Usher et al., 2003; Wagner et al., 2008). Dust aerosol may promote photocatalytic reactions of inorganic gases such as SO₂ and NO₂, initiating nucleation events (Dupart et al., 2012; Nie et al., 2014).

75 The uptake of volatile organic compounds (VOCs) on mineral dust, such as limonene,
76 toluene (Romanías et al., 2016), isoprene (Zeineddine et al., 2017), phenol
77 (Hettiarachchi and Grassian, 2024), and dicarboxylic acids (Ponczek et al., 2019), is
78 also documented. These reactions may alter the VOC budget in the atmosphere and
79 lead to the formation of secondary organic aerosols (SOA) (Li et al., 2019; Tang et al.,
80 2017; Usher et al., 2003; Xu et al., 2023; Zeineddine et al., 2023), one of the key
81 players of atmospheric chemistry (Shrivastava et al., 2017).

82 Glyoxal (CHOCHO) is one of the most abundant VOCs in the troposphere (Lewis et
83 al., 2020). It is produced through the oxidation of aromatic compounds like benzene,
84 toluene, and p-xylene (Volkamer et al., 2001) as well as by the photochemical oxidation
85 of isoprene (Chan et al., 2017). The global atmospheric concentrations of glyoxal have
86 been evaluated in the range of 10 – 100 pptv by Fu et al. (2008). However, case studies
87 show sometimes higher concentrations. During a field study in Shanghai in the summer
88 of 2018, Guo et al. (2021) reported an average glyoxal concentration of 164 ± 73 pptv,
89 due to daytime photochemistry. Local concentrations of up to 400 pptv have been
90 documented in regions influenced by aromatic pollution (Li et al., 2022). Satellite
91 measurements of glyoxal show that the highest concentrations in tropical and sub-
92 tropical regions are found during warm, dry periods influenced by biogenic emissions
93 and vegetation fires, but also anthropogenic pollution (Vrekoussis et al., 2009).
94 Elevated glyoxal concentrations have been observed in aged biomass burning plumes
95 and tropical ocean regions, revealing model under-predictions in high-emission areas
96 due to missing complex organic compound sources (Kluge et al., 2023). Field
97 measurements in the northeast Atlantic Ocean reveal that models generally
98 underestimate glyoxal concentrations due to missing contributions from acetaldehyde
99 and other chemical precursors, and a potential glyoxal source from the ocean surface
100 organic microlayer, particularly significant at night (Walker et al., 2022).

101 Glyoxal is a very soluble molecule which readily oligomerises in water, leading to the
102 formation of larger molecules (Kalberer et al., 2004; Shapiro et al., 2009). Several
103 previous studies have revealed that glyoxal can be taken up onto aerosol particles,
104 potentially serving as a significant source of organic aerosols (e.g., Liggio et al., 2005b;
105 Carlton et al., 2007; Ervens and Volkamer, 2010; Galloway et al., 2009; Knote et al.,
106 2014). The uptake of glyoxal on ammonium sulphate particles can lead to the formation
107 of carbon-nitrogen compounds (such as imidazole derivatives), oligomers, and organic

108 acids (Galloway et al., 2009), that has been observed to cause browning (De Haan et
109 al., 2020). The light-absorbing imidazole derivatives formed by glyoxal have been
110 found to act as a photosensitizer, initiating radical chemistry under realistic irradiation
111 conditions in the aerosol phase and initiating aerosol growth in the presence of
112 limonene (Rossignol et al., 2014).

113 The study by Shen et al. (2016) revealed that glyoxal can also uptake onto synthetic
114 minerals proxies of natural mineral dust, forming oligomers, organo-sulphates, formic
115 acid, and glycolic acid, henceforth suggesting a potential significant mechanism for
116 organic aerosol formation and modification of the optical and hygroscopic properties of
117 mineral dust. Recently, Zogka et al. (2024) highlighted the dependence of the soil
118 composition and size for the uptake of glyoxal on soils and soil surrogates (synthetic
119 mineral).

120 Following up from those studies, in this paper we present novel laboratory experiments
121 using a large-scale simulation chamber to investigate the formation of organic aerosol
122 from the uptake of glyoxal on realistic airborne mineral dust particles, in
123 atmospherically-relevant conditions. Dust aerosols are generated from a natural parent
124 soil from the Gobi Desert, one of the most important sources of tropospheric dust and
125 representative of an area where this interaction could take place (Wang et al., 2015).

126 This paper has two major objectives. First, it provides experimental observations of the
127 uptake of glyoxal on mineral dust aerosol, leading to the formation of organic aerosol
128 mass upon interaction and measuring glyoxal uptake coefficient of mineral dust.
129 Secondly, it presents the chemical composition of the mixed organic-dust aerosols, in
130 terms of their oxidation state, molecular composition and the evolution of SOA content
131 from glyoxal.

132 **2. Experiments and methods**

133 This study uses the CESAM atmospheric simulation chamber (CESAM – Chambre de
134 Simulation Atmosphérique Multiphasique, which translates to Experimental
135 Multiphase Atmospheric Simulation Chamber in English), a 4.2 m³ cylindrical
136 stainless-steel reactor initially described by Wang et al. (2011). CESAM was
137 specifically designed to study multiphase processes involving aerosol particles, gas-
138 phase compounds and water, both in the vapour and liquid phases (Brégonzio-Rozier
139 et al., 2016; Denjean et al., 2014; Giorio et al., 2017). CESAM is equipped with three

140 6.5 kW high-pressure arc xenon lamps (model EX-170GM3-E, IREM SpA, Borgone,
141 Italy) and 6 mm Pyrex plate filters to mimic the solar radiation. A 50 cm stainless-steel
142 four-blade fan located at the bottom of the chamber ensures a mixing time of about 1
143 minute for the gas phase and the homogeneity of the internal composition.

144 **2.1. Injection and cleaning protocols**

145 Dust aerosols were generated and injected into the chamber according to the protocol
146 detailed in Battaglia et al. (2025) using a natural soil sample from the Gobi Desert
147 (107.48°N; 36.49°E). Prior to use, the soil was sieved at 1000 µm and dried at 100°C
148 for less than one hour to remove adsorbed water and contamination from volatile
149 gases. The sediment was sieved to 100 µm. A quantity ranging from 30 and 50 g was
150 placed in a 1 L Büchner flask and shaken at 100 Hz using a sieve shaker (Retsch®
151 AS200) to simulate the saltation and sandblasting mechanisms through which wind
152 erosion generates airborne dust in the real atmosphere (Di Biagio et al., 2017). An
153 Aerodynamic Aerosol Classifier (AAC, Cambustion®) was placed between the dust
154 generator and the chamber to inject mono-modal dust centred between 300 and 400
155 nm in geometric diameter.

156 Glyoxal was prepared by heating a mixture of equal amounts of its trimer hydrate
157 (Fluka® Analytical) and P₂O₅ (Sigma – Aldrich ReagentPlus®, 99%) at 150°C (Horowitz
158 et al., 2001). The trimer decomposition occurs inside a vial connected to a vacuum gas
159 manifold. Glyoxal was collected as yellow crystals in a second vial immersed in an
160 ethanol – liquid nitrogen cold trap at around -90°C and then vaporised in a 2.1 L glass
161 bulb to a controlled pressure. This vial was connected to the simulation chamber to
162 inject the glyoxal through a pure nitrogen flow.

163 Ozone was generated by a Corona discharge in pure O₂ using a commercial dielectric
164 ozone generator (MBT 802N, Messtechnik GmbH, Stahnsdorf, Germany). Water
165 vapour was generated by heating ultrapure water (Milli-Q IQ 7000, Merk™) inside a
166 pressurised stainless-steel vessel, previously rinsed at least three times. The total
167 organic carbon (TOC) content of the ultrapure water was monitored to evaluate the
168 influence on the production of organic particles, which was found to be minor (see **Text**
169 **S1** and **Figures S1 and S2** in the Supplementary Material). The relative humidity (RH)
170 inside the chamber was measured by a HMP234 Vaisala® humidity and temperature
171 transmitter. Before each experiment, the chamber was evacuated down to 10⁻⁴ mbar

and then filled with a mixture of 80% N₂ (Messer, purity > 99.995%) and 20% O₂ (Linde 5.0, purity 99.999%) to an internal pressure exceeding by about 5 to 10 mbar the room atmospheric pressure, to prevent accidental contamination during the experiments.

2.2. Instrumentation

The CESAM chamber was equipped with a suite of standard instrumentation for the detection of the aerosol and the gas phase, whose details are reported in **Table S1**.

Gas-phase glyoxal was measured by a combination of in-situ long-path Fourier Transform Infra-Red (FTIR) spectrometry (Bruker Tensor 37) in the 2720-2930 cm⁻¹ absorption band corresponding to the C–H bonds, by a Cavity Attenuated Phase Shift (CAPS) NO₂ analyser (Model T500U, from Teledyne API) and a Proton Transfer Reaction-Time Of Flight-Mass Spectrometer (PTR-ToF-MS) (KORE Technology®, second generation) operated in H₃O⁺ ionization mode for VOC detection. The FTIR spectrometer also provided the concentrations of formic acid (HCOOH), measured in the C–O bond vibration band centred at 1105 cm⁻¹; ozone (O₃), measured in the asymmetric stretching of the absorption band centred at about 1043 cm⁻¹; and carbon monoxide (CO), detected at about 2143 cm⁻¹. The standard infrared absorption spectra of the compounds used for quantification, along with the specific absorption bands integrated for their quantification, are shown in **Figure S3**. CO and carbon dioxide (CO₂) were additionally measured by an APEE ProCeas® analyser. Nitrogen oxides (NO_x) were monitored by the APNA-370 analyser by Horiba®.

The aerosol total number concentration above 2.5 nm was measured by a Condensation Particle Counter (TSI® model 3075). The aerosol number size distribution in the submicron fraction was measured by a combination of a Scanning Mobility Particle Sizer (SMPS) consisting of a Differential Mobility Analyser (TSI®, model 3080) coupled with a Condensation Particle Counter (TSI® model 3072) and an Optical Particle Counter (sky-GRIMM® OPC model 1.109).

The aerosol chemical composition was measured by a combination of online and offline methods. A Time-of-flight Aerosol Chemical Speciation Monitor (ToF–ACSM, Aerodyne Research Inc.) equipped with a standard vaporiser provided quantitative unitary mass resolution spectra between 40 nm and 1 µm vacuum aerodynamic diameter (Fröhlich et al., 2013). The instrument was operated through a Nafion membrane dryer (model PD-50T-12). The organic mass concentration (m_{org}) was

obtained considering a unitary collection efficiency ($CE = 1$) and a relative ionization efficiency (RIE) of 1.4 (Nault et al., 2023).

The glyoxal fragment CH_2O^+ at m/z 30 has an isobaric interference with the NO^+ fragment from nitrate. Following Galloway et al. (2009), the contribution of nitrate to the total signal at m/z 30 was calculated as 1.7 times the intensity of the nitrate signal at m/z 46, which corresponds to the 30/46 signal ratio measured during nitrate calibration. The contribution to m/z 30 of glyoxal was then calculated from the total signal by subtracting the contribution of the nitrate and the contribution of air. The elemental ratios of the organic fraction O/C and H/C are calculated from the measured f_{44} and f_{43} , respectively, following the parametrizations proposed by Aiken et al. (2008) and Ng et al. (2011), respectively.

Filter samples were collected on PTFE filters (Zefluor, 47 mm diameter, 2 μm pore size, Pall Life Sciences) and quartz fiber membranes (Tissuquartz 2500 QATUP, 47 mm diameter, Pall Life Sciences) using a series of custom-made stainless-steel holder of 6-mm diameter operated at 10 L min^{-1} , and preceded by an denuder filled with active charcoal paper to remove ozone and VOCs. The sampling time ranged from 30 minutes to 3 hours. The filter holders and PTFE filters were pre-cleaned with dichloromethane (99.8 %, HPLC grade) in an ultrasonic bath, while the quartz filters were pyrolyzed at 550°C for approximately 8 hours. After sampling, filters were folded and placed in an aluminium paper envelope previously pyrolyzed (same protocol as the filters) and stored in a refrigerator at -18°C. Chamber blanks were collected by sampling for about 20 min from the chamber only filled with N_2 and O_2 . Analytical blanks were also collected.

2.3. Filter analysis

The analysis of the filter samples was conducted by a combination of three techniques to provide a comprehensive view of the chemical composition of the organic fraction formed on the dust particles as the result of the processing by glyoxal. The full details of the analysers and analytical protocols are reported in as detailed in **Text S2** in the supplementary material. Those include

- 1/ the Supercritical fluid extraction coupled with gas chromatography mass spectrometry (SFE/GC-MS; Chiappini et al. (2006)) for target analysis of low-weight mass fragments derived from molecules linked to glyoxal reactivity (see

Table S2.1 in the Supplementary Material). such as the m/z 131 fragment (Glyoxylic acid TMS derivatized – CH₃), and the m/z 205 fragment (Glyoxal monohydrate – CH₃);

2/ Electrospray ionization (ESI) high-resolution mass spectrometry (Kourtchev et al., 2015) was used to obtain high-resolution mass spectra and formulae assignments for low-volatility compounds in the ranges m/z 50–500 and m/z 150–1000 (Zielinski et al., 2018). These were processed to provide parameters describing the carbon oxidation, through O/C and H/C bulk ratios, and the identification of molecular groups such as CHO, CHON, CHOS, CHNS, and CHONS. ESI-HR-MS was also used for a screening analysis of molecules resulting from the glyoxal transformation due to hydration, oxidation, and oligomerization. These included formulas for mono- and dihydration products (C₂H₄O₃ and C₂H₆O₄, respectively), oxidation products (formic acid (CH₂O₂), glycolic acid (C₂H₄O₃), glyoxylic acid (C₂H₂O₃), and oxalic acid (C₂H₂O₄)), and oligomers formed by the hydrolysis of hydrated glyoxal formulas (linear oligomers with generic stoichiometric formula C_{2n+2m}H_{4n+6m-2(n+m-1)}O_{3n+4m-(n+m-1)}, and ring oligomers with generic formulae C_{2n+2m}H_{4n+6m-2(n+m)}O_{3n+4m-(n+m)}).

3/ X-ray photoelectron spectrometry (XPS) was used following Denjean et al. (2015) to quantify the elemental O/C ratio of the particle surface (O/C_{surf}) to a depth of less than 10 nm. The O/C_{surf} was calculated as explained in Text S2 in the Supplementary Material. The XPS measurement on a filter collected during one ageing experiment is shown as an example in **Figure S4** in the Supplementary Material.

2.4. Calculation of the aerosol size distribution

The procedure for combining the measurements of the SMPS and the sky-GRIMM® OPC is based on Baldo et al. (2023) and described in detail in Battaglia et al. (2025). The number size distributions, expressed in dN/dlogD (cm⁻³), are used to evaluate the total particle surface S (μm² cm⁻³) and volume V (μm³ cm⁻³) by assuming spherical particles as

$$S = \int \pi D^2 \frac{dN}{d\log D} d\log D \quad (2)$$

$$V = \int \frac{\pi}{6} D^3 \frac{dN}{d\log D} d\log D \quad (3)$$

2.5. Calculation of the glyoxal uptake coefficient and rate of particle formation

The uptake coefficient (γ) is defined as the probability of the gas to be taken up on the aerosol surface. It is a unit-less parameter expressed by the ratio between the number of molecules taken up on a surface and the total number of collisions of the gas on the surface as

$$\gamma = \frac{\text{number of total molecules taken up}}{\text{total number of collisions}} \quad (4)$$

The gas-phase uptake coefficient (γ) was estimated from the first-order heterogeneous loss rate of glyoxal (k_{het} , s⁻¹) as

$$\gamma = \frac{k_{het}}{\omega} \quad (5)$$

The rate of collisions (collision frequency, ω) is defined as

$$\omega = \frac{cA_s}{4} \quad (6)$$

where:

- $c = 146 \times \sqrt{\frac{T}{MW}}$ is the mean molecular speed (m s⁻¹), where T is the air temperature (here 298 K) and MW the molecular weight of the compound of interest (in the case of glyoxal MW = 58 g mol⁻¹).

- A_s is the total aerosol surface concentration (m² m⁻³).

The total aerosol surface concentration (A_s) is calculated from the aerosol size distribution recorded at the end of the dust injection.

The heterogeneous loss rate of glyoxal (k_{het}) due to its uptake on dust particles can be determined as the difference between the loss rate of glyoxal measured during the uptake experiments (k_{obs}) and the glyoxal loss rate on the chamber walls (k_{loss}) as

$$k_{het} = k_{obs} - k_{loss} \quad (7)$$

The glyoxal wall loss is represented by a partition equilibrium described by two first-order reactions: one for the adsorption of gas-phase molecules onto the chamber walls, and one for the reverse process. The rate constants for both processes have been obtained experimentally through control experiments with only glyoxal in the chamber and at different relative humidity conditions, as detailed in **Text S3** and Figures S5 to S9 in the supplementary material.

If the uptake reaction is of the first rate, k_{het} is henceforth calculated as

$$k_{het} = \frac{\ln\left(\frac{[Gly]_0}{[Gly]_{obs}}\right) - \ln\left(\frac{[Gly]_0}{[Gly]_{loss}}\right)}{t} \quad (8)$$

where $[Gly]_0$ is the initial concentration of glyoxal, $[Gly]_{obs}$ represents the observed evolution of glyoxal concentration in time, resulting from the sum of uptake and wall loss, and $[Gly]_{loss}$ represents the estimated glyoxal concentration resulting from the wall loss.

The rate of formation of the particulate organic matter (POM; k_{F-POM}) due to the uptake of glyoxal on the dust can be calculated as

$$k_{F-POM} = \frac{\ln\left(\frac{[POM]_t}{[POM]_0}\right)}{t} \quad (9)$$

where $[POM]_0$ represents the initial POM concentration in the particle phase, and $[POM]_t$ represents the concentration of the POM formed at a given time.

In the hypothesis that the POM formation is solely due to the uptake of glyoxal, γ can also be evaluated as

$$\gamma = \frac{k_{F-POM}}{\omega} \quad (10)$$

3. Results and discussion

3.1. Overview of experiments

The ageing experiments of monodispersed mineral dust and glyoxal described in this paper are summarised in **Table 1**. All the aerosol data are corrected for dilution, wall loss, and particle loss through the tubing systems as detailed in **Text S4** and Figures S10 and S11 in the Supplementary Material. Gas phase concentrations are corrected for dilution only.

Table 1. Listing and initial conditions of the experiments considered in this study, including experiments with glyoxal only (experiment type GL), ammonium sulphate and glyoxal (AS + GL), dust only (D) and dust with glyoxal (D + GL). The glyoxal and ozone gas phase concentrations correspond to the maximum value measured by FTIR after the respective injections. V_{seed} indicates the maximum volume concentrations of seed particles (either dust or ammonium sulphate) measured after the particle injection. The notation “dark/light” indicates experiments when filter samples were collected both in the dark and with irradiation.

Experiment type	Reagents	Date	Experiment number	RH, %	Light	[O ₃], ppb _v	Temp, K	[GL], ppb _v	V _{seed} , μm ³ cm ⁻³	
Control	GL	29/04/2021	G ₁	< 5	dark	---	292	1130	---	
		11/02/2022	G ₂	77	light	1440	291	627	---	
	AS+GL	21/02/2023	AS ₁	38	dark	---	298	527	50.1	
		23/02/2023a	AS ₂	35	dark	---	298	516	48.3	
		23/02/2023b	AS ₃	32	light	---	298	445	64.8	
		07/09/2023	AS ₄	81	light	---	301	779	304.1	
		08/09/2023	AS ₅	83	light	---	300	430	161.2	
		D	31/01/2022	D ₁	< 5	dark/light	---	292	---	31.5
	03/02/2022		D ₂	75%	dark/light	---	293	---	55.4	
	Uptake	D+GL	04/02/2022	D ₃	< 5	dark/light	---	293	690	35.6
			08/02/2023	D ₄	32	dark	---	294	940	21.5
09/02/2023			D ₅	31	light	---	295	1050	52.7	
10/02/2023			D ₆	35	dark	---	294	809	37.4	
13/02/2023			D ₇	34	light	---	296	850	51.3	
30/04/2021			D ₈	76	light	---	289	759	28.3	
03/05/2021			D ₉	79	light	---	290	607	38.7	
04/05/2021			D ₁₀	81	light	---	290	371	31.5	
05/05/2021			D ₁₁	78	dark	---	291	805	30.1	
06/05/2021			D ₁₂	82	dark	---	292	432	21.1	
08/02/2022			D ₁₃	81	dark/light	1270	293	555	64.0	
09/02/2022	D ₁₄		78	dark/light	1450	293	756	79.8		
10/02/2022	D ₁₅		75	dark/light	---	295	600	68.4		
14/02/2023	D ₁₆	83	dark	---	296	661	35.8			
15/02/2023	D ₁₇	75	light	---	298	444	41.0			

Table 1 also lists the few control experiments using ammonium sulphate as seed particles, described in detail in **Text S5** and Figures 12 to 14 in the Supplementary Material. No POM formation was observed during control experiments with dust or glyoxal only, both dry and humid conditions and with and without irradiation.

3.1.1. Timeline of particle concentration and composition

The ageing experiments lasted up to five hours. For the experiments carried out in wet conditions, the injection of water vapour preceded the injection of dust. The injection of glyoxal (nominal concentration of 1 ppmv) was conducted at least 30 minutes after the dust to ensure that the dust particles were homogeneously distributed in the reactor. Irradiation was started within one hour after the glyoxal uptake onto the particles. In a few experiments, ozone was injected before glyoxal to verify the sensitivity of the reactions to the presence of an oxidant.

The typical timelines of the particle concentrations (number and volume) and the non-refractory composition measured in dry conditions and at 30% and 80% relative humidity are shown in **Figure 1**.

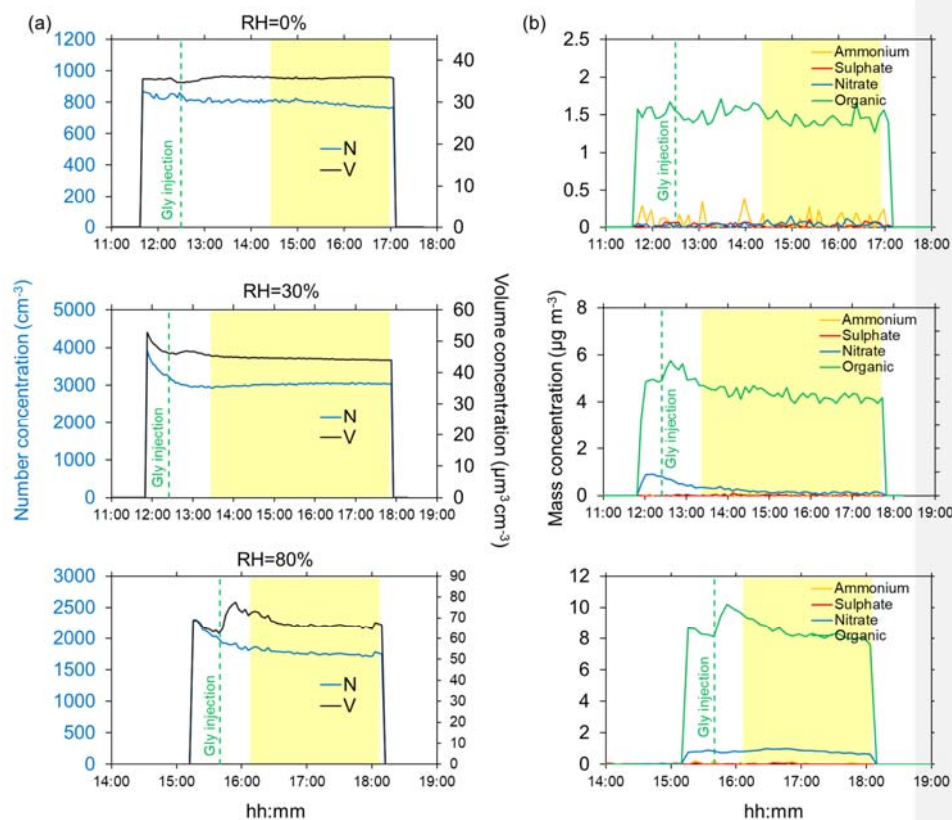


Figure 1. Timeline of ageing experiments of submicron dust with gas-phase glyoxal in dry conditions (top, experiment D₃), 30% (middle, experiment D₇), and 80% RH (bottom, experiment D₁₅). Left (a): aerosol total number (N) and volume (V) concentrations (blue and black lines, respectively) calculated from the measured dust size distributions. Right (b): mass concentrations of ammonium, sulphate, nitrate and organic (yellow, red, blue and green lines, respectively) measured by the ACSM. The yellow-highlighted portion of the graph indicates the interval where irradiation takes place, while the green vertical dashed lines indicate the injection of glyoxal in the chamber. The dust injection corresponds to the time of the initial increase of the number and volume concentrations. Aerosol time series are corrected for dilution, wall loss and particle loss through the tubings.

Figure 1 shows that in dry conditions, there is no significant variation of either the aerosol number or the volume concentrations, nor the chemical composition (including organics) following the glyoxal injection.

At 30% RH, a small increase in the total volume concentration (approximately $5 \mu\text{m}^3 \text{cm}^{-3}$) is observed for about 30 minutes after the injection of glyoxal. This corresponds to an increase of the POM of about $1 \mu\text{g m}^{-3}$, approximately 20% more with respect to

the value measured before the uptake. On the other hand, the particle number concentration shows an apparent decrease at the beginning of the experiments, possibly because the particle loss correction model of Lai and Nazaroff (2000) does not fully apply to dust particles and humid conditions (see discussion in Battaglia et al. (2025)). After that, and through the duration of the experiment, however, it remains constant, indicating that the increase in the particle volume occurs on the dust particles and not because of new particle formation.

At 80% RH, the increase in both the total volume and the POM concentrations is more pronounced, approximately $10\text{--}15\ \mu\text{m}^3\ \text{cm}^{-3}$ and $2\ \mu\text{g}\ \text{m}^{-3}$, respectively. As for 30% RH, both total particle volume and the POM concentrations return to values observed prior to the injection of glyoxal, within approximately 30 minutes from their maximum values, likely due to evaporation. A similar behaviour is observed in the presence of ozone (**Figure S15** in the Supplementary Material). As for 30% RH, the particle number concentration slightly decreases in time at the beginning of the experiment, but then remains constant, again excluding the formation of new particles but rather confirming the formation of organic matter on pre-existing particles. This is also supported by the fact that the rate of increase of POM and particle volume is the same (slope $3.2 \times 10^{-4}\ \text{s}^{-1}$ and $3.2 \times 10^{-4}\ \text{s}^{-1}$, respectively, for POM and total volume), as shown by **Figure S16** in the Supplementary Material.

3.1.2. Timeline of gas-phase concentration

Figure 1 also shows that, while sulphate and ammonium are never detected, a background concentration of nitrate up to $1\ \mu\text{g}\ \text{m}^{-3}$ is measured by the ACSM as soon as the dust particles are injected in the presence of water. We attribute it to the heterogeneous interaction between NO_2 and the dust particles (Goodman et al., 1999), as indeed, a background concentration of a few ppb of NO_2 is present in the chamber as a result of the procedure used to reduce the TOC content in the injected water (see **Figure S17** in the Supplementary Material). However, since the contribution of nitrate represents at maximum 1% of the injected dust mass and it decreases or remains constant throughout the experiment, its contribution to the particle growth and overall ageing of the mineral dust should be negligible.

Figure 2 shows the time series of the gas-phase compounds detected during the same experiment (D_{15}) at 80% RH.

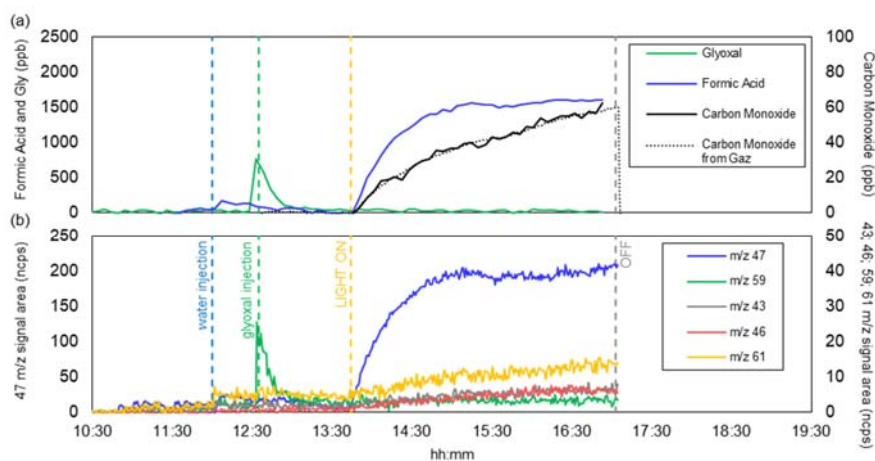


Figure 2. Time series of the gas-phase composition observed during experiment D₁₅: (a) concentrations of carbon monoxide, glyoxal and formic acid measured by FTIR (for CO, the measurements of the online analyser are also shown); (b) various VOC ions (m/z 47, 59, 43, 46 and 61) measured by the PTR-MS. Ion signals measured by PTR-MS are normalized by signals of reagent ions (i.e. H_3O^+ and $H_3O^+(H_2O)$) and therefore expressed in normalized counts (ncps). The blue vertical dashed lines indicate the injection of water in the chamber; the green vertical dashed lines indicate the injection of glyoxal in the chamber, the yellow dashed lines indicate the beginning of irradiation, and the grey dashed lines indicate the end of irradiation.

The measured glyoxal concentration after the injection (**Figure 2a**) is lower than the nominal concentration of 1 ppm and goes to zero within minutes due to the rapid interactions with the walls of the chamber, water vapour, and the dust particles. Upon irradiation, formic acid and carbon monoxide are formed, as expected by the photolysis of glyoxal (De Haan et al., 2020). Fragments $m/z = 46$ and 47 are observed during water injection and photolysis, which could originate from the deprotonated and protonated form of formic acid, respectively. This suggests that a minor fraction of the formic acid could result from the desorption of compounds (including glyoxal) from the chamber walls. Fragments $m/z = 43$ and $m/z = 61$, and occasionally $m/z = 45$ (not seen during experiment D₁₅ and therefore not shown in **Figure 2b**), are observed at a normalised intensity two orders of magnitude lower than that of formic acid, but not attributed. The quantification with both PTR-MS and FTIR in our experimental RH conditions is complex due to water presence, which reduces the sensitivity of PTR-MS and can interfere with the absorption of various organic compounds, making their quantification less accurate.

3.2. Evaluation of glyoxal uptake coefficient and rate of formation of organic aerosols

Figure 3 shows an example of the temporal evolution of the natural logarithm of the glyoxal concentration measured by the FTIR, compared to that measured during a typical blank experiment without dust particles (top panel) and the variation of the aerosol organic fraction measured by the ToF-ACSM during the same time period (lower panel).

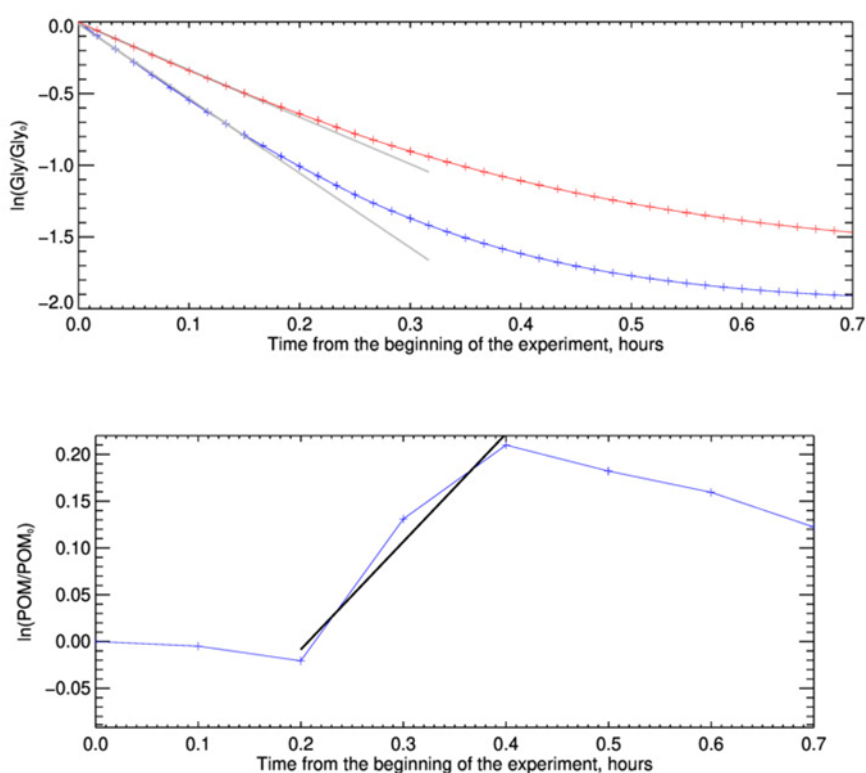


Figure 3. Measurement of glyoxal uptake coefficient on dust for the experiment D₁₅, conducted at 80% RH. The figure compares the two methods for measuring the uptake coefficient. In the top image, results are shown for the method based on monitoring the decay of gas-phase glyoxal. The red and blue curves represent the logarithm of the ratio between the calculated decay of gas-phase glyoxal in the absence and presence of dust aerosols, respectively. The black lines represent the linear fit whose slope provides the heterogeneous kinetic constants of the two processes. The image at the bottom displays the result of the uptake coefficient measurement for the same experiment, obtained from the organic formation on the dust aerosol monitored by the ToF-ACSM. The blue time series shows the logarithm of the ratio between the measured organic concentration divided by the initial organic on dust aerosol, while the black line is the linear fit representing the kinetics of organic formation.

Within the first 10 minutes after the injection of glyoxal, the decrease of the natural logarithm concentrations ratio with time in the presence of dust is linear (that is, the rate is constant). After that, the loss slightly deviates from linearity. The difference from linearity is more evident for the blank experiment, when it occurs earlier than when the dust is present. These observations indicate that, within the first 10 minutes, the uptake of glyoxal on the dust particles can be considered to follow a first-order kinetics and its rate represents an initial uptake coefficient. In the following 20 minutes approximately, the uptake slows down, possibly because all the sites available on the particle surface become occupied, but also because that desorption from the particle surface could reinject glyoxal into the reactive mixture. On the particle phase, the natural logarithm of the organic concentration, normalised by its initial value, increases rapidly and linearly, almost on the same time scale as that of the loss of glyoxal, but then decreases to return to its initial value within approximately one hour. These observations confirm that the uptake of glyoxal results in the formation of OA on the dust particles, but that this process is reversible.

The uptake coefficients calculated as the linear fit of the glyoxal and particle organic concentration are presented in **Table 2**.

Table 2. Uptake coefficients for glyoxal on mineral dust and ammonium sulphate calculated from the loss of gas-phase glyoxal ($\gamma_{\text{Gly-Dust-gas}}$) and the rate of OA formation ($\gamma_{\text{Gly-Dust-gas}}$) for the experiments conducted at 80% RH. The initial glyoxal concentration is reported. The aerosol surface concentration (A_s) corresponds to the value preceding the glyoxal injection. Ozone concentration is the maximum concentration measured by FTIR spectroscopy after the injection. For ammonium sulphate, only the γ values calculated from the loss of gas phase glyoxal are presented, as the ACSM collection efficiency (CE) for ammonium sulphate varies significantly during OA formation (Matthew et al., 2008).

Date	Experiment ID	RH%	[GL] ₀ , ppbv	Ozone (ppb)	A_s ($\text{m}^2 \text{m}^{-3}$)	ω (s^{-1})	$\gamma_{\text{Gly-Dust-gas}}$	$\gamma_{\text{Gly-Dust-OA}}$
30/04/2021	D ₈	76	759	---	4.8×10^{-4}	3.9×10^{-2}	6.0×10^{-3}	1.0×10^{-3}
03/05/2021	D ₉	79	607	---	6.1×10^{-4}	5.0×10^{-2}	1.5×10^{-2}	1.5×10^{-2}
04/05/2021	D ₁₀	81	371	---	5.1×10^{-4}	4.2×10^{-2}	1.7×10^{-2}	9.0×10^{-3}
05/05/2021	D ₁₁	78	805	---	4.6×10^{-4}	3.8×10^{-2}	8.0×10^{-3}	5.0×10^{-3}
06/05/2021	D ₁₂	82	432	---	3.5×10^{-4}	2.9×10^{-2}	1.2×10^{-2}	2.3×10^{-2}
08/02/2022	D ₁₃	81	555	1270	7.1×10^{-4}	5.8×10^{-2}	4.0×10^{-3}	4.0×10^{-3}
09/02/2022	D ₁₄	78	756	1450	8.5×10^{-4}	7.0×10^{-2}	4.0×10^{-3}	5.0×10^{-3}
10/02/2022	D ₁₅	75	600	---	8.4×10^{-4}	6.9×10^{-2}	1.0×10^{-2}	5.0×10^{-3}
14/02/2023	D ₁₆	83	661	---	6.0×10^{-4}	4.9×10^{-2}	4.0×10^{-3}	1.5×10^{-2}
07/09/2023	AS ₄	81	779	---	6.3×10^{-3}	5.2×10^{-1}	9.8×10^{-4}	---
08/09/2023	AS ₅	83	430	---	2.0×10^{-3}	1.7×10^{-1}	1.2×10^{-3}	---
Average dust							$9 (\pm 5) \times 10^{-3}$	$9 (\pm 7) \times 10^{-3}$
Average AS							$1.1 (\pm 0.2) \times 10^{-4}$	

474

475 The average uptake coefficients for glyoxal on the Gobi mineral dust calculated at 80%
476 RH from the gas-phase uptake and the particle formation are $\gamma_{\text{Gly-Dust-gas}} = 9 \times 10^{-3}$
477 (standard deviation ± 5) and $\gamma_{\text{Gly-Dust-OA}} = 9 \times 10^{-3}$ (standard deviation ± 7), respectively.
478 The two average values agree. This suggests that every glyoxal molecule in the gas
479 phase is taken up by the airborne dust particles. This also suggests that the uptake
480 occurs on airborne particles only, as expected, as the dust particles are selected in the
481 submicron range and that minimal deposition of dust particles is observed in the first
482 30 minutes after injection. The primary mechanism of particle loss during this period is
483 dilution, which does not interfere with uptake. The standard deviations of the mean
484 values are large, being attributed to the fact that the state of the chamber walls and the
485 dust size distribution vary from one experiment to the other, and that the
486 aerosol/chamber walls surface ratio is very low ($0.08\text{--}1.5 \times 10^{-3}$).

487 The presence of ozone appears to be unimportant. Hanish and Crowley (2003a)
488 investigated the combined uptake of O_3 and HNO_3 onto dust and showed that the
489 uptake of HNO_3 on dust was not influenced by the presence of O_3 (and conversely, the
490 uptake of O_3 was not influenced by the presence of HNO_3). These authors attributed
491 these observations to the fact that in their experiments, O_3 concentrations were in
492 excess by more than three orders of magnitude with respect to those of HNO_3 ,
493 compensating for the fact that the uptake coefficients for O_3 is approximately four
494 orders of magnitude lower than for HNO_3 (Hanish and Crowley 2003b; Chang et al.,
495 2005). In these conditions, which are not generally met in the atmosphere, the
496 presence of O_3 could result in the modification of surface chemical characteristics or
497 competition for adsorption sites of the two species. These considerations are
498 applicable to our experiments, as the uptake coefficients of O_3 and glyoxal are of
499 comparable magnitudes, and we use comparable concentrations.

500 3.3. Evidence of irreversible particle growth

501 **Figure 1** shows that, even in the more favourable conditions (RH=80%), the ratio
502 between the observed increase of the POM ($2 \mu\text{g m}^{-3}$) and that of the particle volume
503 concentration ($20 \mu\text{m}^3 \text{cm}^{-3}$) corresponds to an estimated mass density of the order of
504 0.1 g cm^{-3} , which is about 10 times lower than the value of 1 g cm^{-3} expected for glyoxal.
505 This is partially attributed to the fact that only part of the organic matter formed on dust

506 is detected by the ACSM. On the other hand, **Figure S16** shows that, after reaching
507 its maximum value, the volume concentration decreases at a lower rate than the POM
508 (slope $3.9 \times 10^{-5} \text{ s}^{-1}$ and $6.1 \times 10^{-5} \text{ s}^{-1}$, respectively). This suggests that an additional
509 process could contribute to the particle volume concentration, partially compensating
510 for the loss of organic matter on the dust particles.

511 This is confirmed by **Figure 4**, which shows the variation in time of the normalised
512 particle volume distributions, at four steps of the experiments performed at 30% RH
513 and 80% RH. Those include prior and glyoxal injection, POM maximum peak value,
514 and the end of the experiment.

515

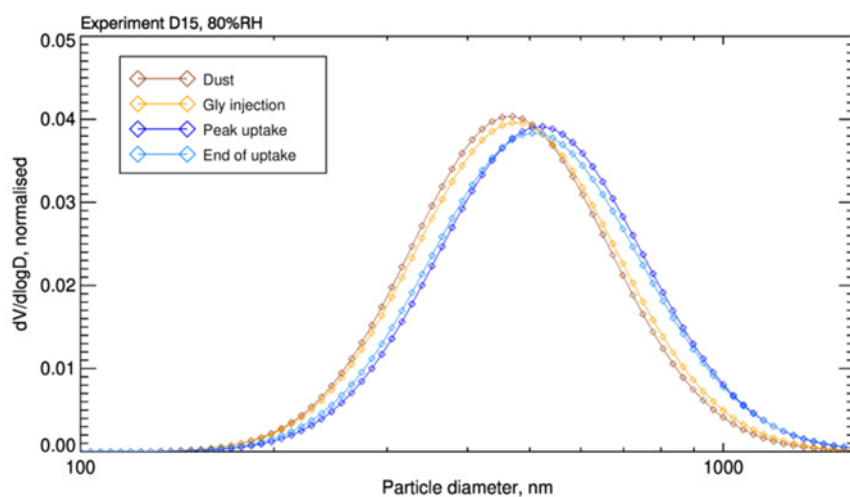
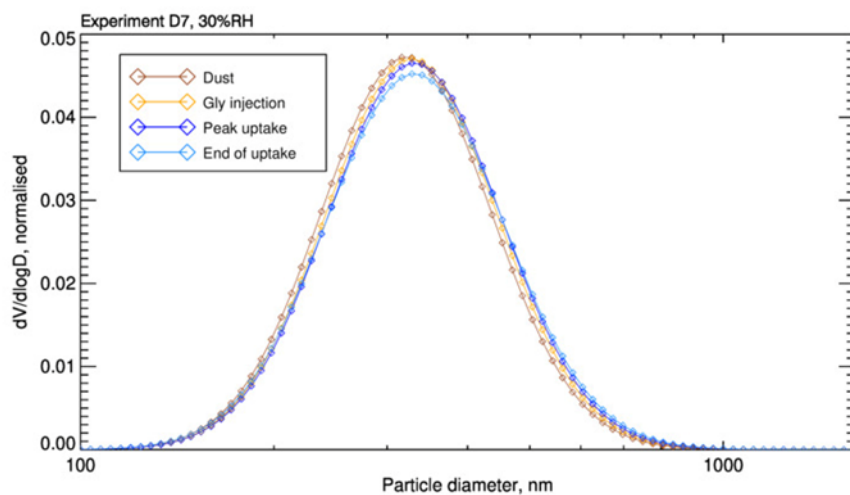


Figure 4. Evolution of volume-size distributions for two glyoxal uptake experiments in different relative humidity conditions. The images illustrate the progression of volume-size distributions recorded at four key moments during the experiments. The first distribution (orange) is recorded after the dust is injected into the simulation chamber. The second distribution (yellow) is recorded at the moment of glyoxal injection. The third distribution (blue) corresponds to the peak uptake of glyoxal on the aerosol, and the fourth (light blue) is recorded at the end of the glyoxal uptake process. The left image depicts the evolution for the experiment D7 conducted at 30% RH, while the image on the right shows the distributions for the experiment D15 conducted at 80% RH. The results highlight that the distributions grow more significantly at 80% RH, indicating a higher glyoxal uptake and organic formation at elevated humidity levels.

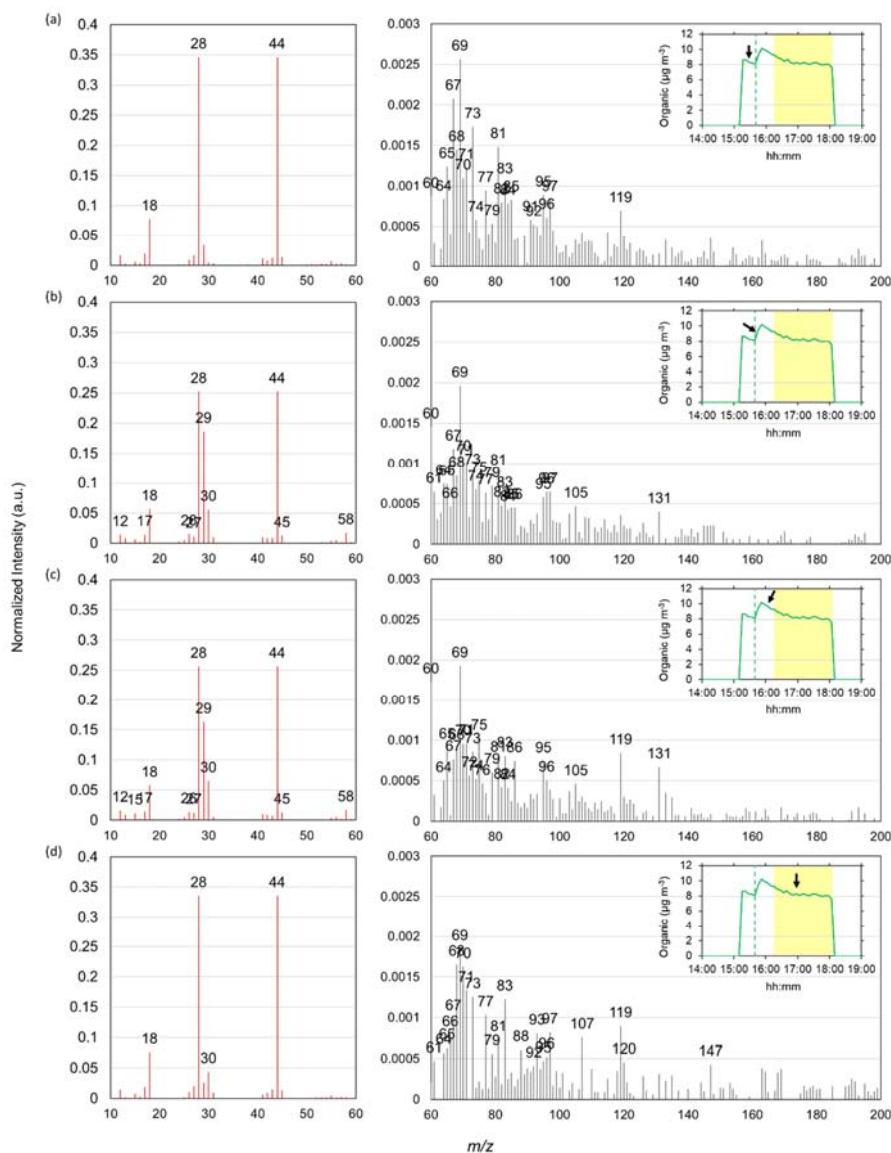
All distributions have a single mode. However, after the injection of glyoxal, the geometric mean volume diameter, measured at the maximum POM concentration, increases by up to 10% (from 310 to 340 nm) at 30% RH, and up to 20% (from 450 to 540 nm) at 80% RH. Interestingly, even at the end of the experiment, when the POM concentration returns to its initial value, the increase in geometric mean diameter of the aerosol is irreversible. We hypothesize that the uptake of glyoxal enhances the dust hygroscopicity. Therefore, the difference in total volume between the beginning and end of the experiment is due to formed organic aerosol mass, resulting from water uptake.

3.4. Chemical composition of the particulate organic matter

This section discusses the chemical composition of the particulate organic matter formed on the mineral dust following the interaction with glyoxal. The list and conditions of the filter samples analysed by SFE/GC-MS and ESI-Orbitrap are reported in **Table S2** in the Supplementary Material. Details of the organic composition of the native dust are provided in **Text S6 and Figures S18 to S20**.

3.4.1. Timeline of chemical evolution

Figure 5 shows the time evolution of the intensity of the organic fragments detected by the ToF-ACSM at 80% RH (experiment D₁₅) at four moments of the experiment: 1) before the injection of glyoxal; 2) during the uptake and the formation of the organic matter; 3) after the organic matter has reached its maximum concentration; and 4) at the end of the experiment, when the organic matter returned to its initial concentration.



550

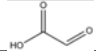
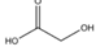
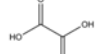
551 **Figure 2.** ACSM organic mass spectra (intensities normalized to the total organic concentration) recorded during
 552 the experiment D₁₅: (a) before glyoxal uptake (dust organic fraction composition), (b) during glyoxal uptake, (c) after
 553 reaching the maximum uptake on the particles and (d) 1h later under irradiation. Panels on the left show the mass
 554 spectra ranging from m/z 10 to 60, while the panels on the right represent fragments from m/z 60 to 200 (their
 555 intensity is approximately one hundred times lower). The inserts display the time series of organic concentrations
 556 measured by the ToF-ACSM. A black arrow indicates the time corresponding to the mass spectrum shown. The
 557 yellow-highlighted shaded area indicates the interval where irradiation takes place, while the green vertical dashed
 558 lines indicate the moment of glyoxal injection in the chamber.

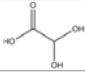
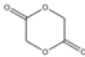
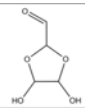
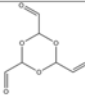
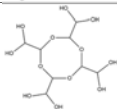
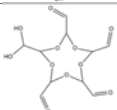
Figure 5 reveals that the organic matter formed as a result of the interaction between mineral dust and glyoxal is composed of oxidized organic fragments, organic acids, and oligomers. Oxidized organic fragments such as CO^+ (m/z 28) and CO_2^+ (m/z 44) are observed through all phases of the experiments. Fragments such as CHO^+ (m/z 29), CH_2O^+ (m/z 30), and $\text{C}_2\text{H}_2\text{O}_2^+$ (m/z 58) appear during the uptake of glyoxal, but diminish over time, due to oligomerization or further oxidation processes. The most intense fragment above m/z 60 is m/z 69, which appears unrelated to glyoxal reactivity but could be attributed to nitrogen-containing organic species such as $\text{C}_3\text{H}_3\text{NO}^+$, originating from glyoxal–ammonia reactions (Galloway et al., 2009) or plant and soil residues (Sun et al., 2010; Nieder et al., 2018). Fragments at m/z 105 and 131, observed consistently during the uptake and the photolysis, could be attributed to condensed glyoxal hydrates (Liggio et al., 2005; Carlton et al., 2007). Fragments at m/z 119 and 120, associated with oxidized products from isoprene-derived aerosols (Safi Shalamzari et al., 2013), increased after glyoxal uptake and under irradiation, suggesting the formation of oxidized oligomers. Upon irradiation, the appearance of m/z 147 and 165 – products of aqueous glyoxal oxidation and oligomer condensation (Lim et al., 2010) – suggests photo-chemically enhanced transformation, though their presence in native dust also points to reversible adsorption processes.

3.4.2. Molecular identification

The list and conditions of the samples analysed by SFE/GC-MS and ESI-Orbitrap are reported in **Text S7** and Figures S21 and S22 in the Supplementary Material, which also provides with examples of analysis. The summary of the organic molecules detected by those analysis is presented in **Table 3**.

Table 3. Summary of observed compounds identified by SFE/GC-MS analysis and glyoxal-related formulas observed with ESI-Orbitrap, along with the suggested structures under the different experimental conditions tested.

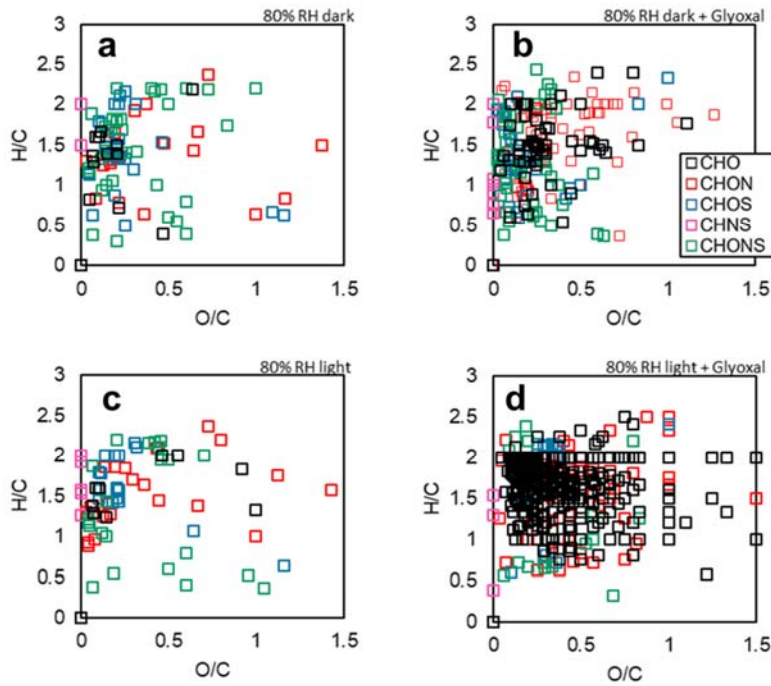
Molecular formula	Name	Tentative Structure	Technique	Experimental conditions
$\text{C}_2\text{H}_2\text{O}_3$	Glyoxylic acid		ESI-Orbitrap	Dust+Gly, 80%, Dark, O_3
$\text{C}_2\text{H}_4\text{O}_3$	Glycolic acid		ESI-Orbitrap SFE/GC-MS	Dust+Gly, 30%, Dark Dust+Gly, 30%, Light Dust+Gly, 80%, Light Dust+Gly, 80%, Light, O_3
$\text{C}_2\text{H}_2\text{O}_4$	Oxalic acid		ESI-Orbitrap	Dust+Gly, 80%, Light

$C_2H_4O_4$	Glyoxylic acid monohydrate		ESI-Orbitrap SFE/GC-MS	Dust+Gly, 80%, Light
$C_4H_4O_4$	Glycolic acid dimer		ESI-Orbitrap	Dust+Gly, 80%, Light
$C_4H_6O_5$	Glyoxal oligomer		ESI-Orbitrap	Dust+Gly, 80%, Light
$C_6H_6O_6$	Glyoxal oligomer		ESI-Orbitrap	Dust+Gly, 80%, Light
$C_8H_{16}O_{12}$	Glyoxal oligomer		ESI-Orbitrap	Dust+Gly, 80%, Light
$C_{10}H_{12}O_{11}$	Glyoxal oligomer		ESI-Orbitrap	Dust+Gly, 80%, Dark

Oxidized organic compounds such as glycolic acid ($C_2H_4O_3$), oxalic acid ($C_2H_2O_4$), and a possible dimer of glycolic acid ($C_4H_4O_4$) were mainly observed under irradiated conditions, while their hydrated forms also appeared in dark conditions. Glyoxylic acid was detected in dark conditions in the presence of ozone. Glycolic and glyoxylic acids consistently form under humid conditions, indicating that their pathways may be less sensitive to water competition or that their precursors interact more strongly with dust surfaces. Light but also ozone tends to favor the formation of glycolic acid from glyoxal at high RH, suggesting two possible oxidative pathways. Glycolic acid is also detected at 30% RH (not showed), with and without irradiation, in agreement with the experiments on dust by Shen et al. (2016), but differently than reported by Galloway et al. (2009) on ammonium sulphate. Monohydrated glyoxylic acid is found in one sample at 80% RH under irradiated conditions, likely due to the known pattern of oxidation of glyoxal and glycolic acid with OH radicals (Buxton et al., 1997). Unlike previous studies (Galloway et al., 2009; Rubasinghege et al., 2013; Shen et al., 2016), formic acid was not detected on the particle phase despite high concentrations observed in the gas phase (**Figure 2**). It can be hypothesized that formic acid was not detected in the particle phase due to the low amount of organic material on the filter samples and the unsuitability of the method used (due to interferences at the retention time where formic acid is expected).

606 Oligomerization products (compounds from C4 to C10) of the glyoxal mono- and di-
607 hydrate forms are observed only at 80% RH. These are: C₄H₆O₅ (1 monohydrated
608 glyoxal + 1 dehydrated glyoxal forming a 5-atom ring), C₈H₁₆O₁₂ (4 dehydrated glyoxal
609 molecules forming an 8-membered ring), and C₁₀H₁₂O₁₁ (4 monohydrated glyoxal
610 molecules + 1 dehydrated glyoxal molecule forming a ring structure). The oligomer
611 C₆H₆O₆ (3 molecules of monohydrated glyoxal forming a 6-membered ring) is detected
612 only under dark conditions. C₈H₁₆O₁₂, can correspond to an oligomer previously
613 observed by Shen et al. (2016) on mineral dust.

614 The persistence of low-volatility, heavy compounds, such as oligomers at the surface
615 of mineral dust has implications for its oxidation state, which is modified in an
616 irreversible way its surface composition, as already shown by previous studies on
617 ammonium sulphate seeds (Kroll et al., 2005; Galloway et al., 2009; De Haan et al.,
618 2020; Hu et al., 2022). This is illustrated by the van Krevelen diagrams obtained from
619 the ESI-Orbitrap analysis in **Figure 6**.



620
621 **Figure 6.** Van Krevelen diagrams recorded at 80% RH for: in the top line experiments in the dark for
622 mineral dust only (control experiment D₂, left) and one ageing experiment of dust with glyoxal

(experiment D10); bottom line: same with irradiation. Samples are equivalent in terms of load of particulate organic matter. These are 0.9 µg (sample a), 0.8 µg (sample b), 1.7 µg (sample c) and 0.6 µg (sample d). Despite an equivalent loading of particulate organic mass, the number of signals detected is significantly higher when the dust is exposed to glyoxal (86 and 102 peaks detected for dust only against 398 and 310 with glyoxal, and with and without light, respectively).

628

The processing by the glyoxal clearly has an effect on the oxidation state of the dust, particularly when lights are on, resulting in the appearance of signals with O/C ratio higher than 1, attributed to photo-oxidation. The predominant family in this case is that of CHO molecules, while the appearance of molecules for families CHON and CHONS is also observed.

634 4. Discussion

635 4.1. Comparison of uptake coefficients

The uptake of glyoxal on the dust particles occurs in humid conditions exceeding 30% RH. These observations agree with the results of Liggio et al. (2005a; 2005b) on the uptake of glyoxal on ammonium sulphate aerosols, observing the formation of organic matter only when RH exceeded 50%. Trainic et al. (2011) also observed that the uptake of glyoxal on glycine and ammonium sulphate particles occurred only when the relative humidity was above 35%. On the contrary, both Shen et al. (2016) and Zogka et al. (2024) demonstrated that the uptake can occur in dry conditions too, which was not observed in this work.

At 80% RH, the experimental average of the measured uptake coefficient of glyoxal on mineral dust is $\gamma = (9 \pm 5) \times 10^{-3}$. Our values are approximately one order of magnitude higher than those obtained by Shen et al. (2016), who investigated the uptake of glyoxal on mineral proxies, i.e. SiO₂, CaCO₃ and α -Al₂O₃ under various levels of RH. These authors determined the uptake coefficients after a long exposition of the surface to glyoxal (steady state uptakes) and found that the uptake coefficients decrease with increasing gas phase concentration of glyoxal. At 1 ppb concentration and 60% RH, the uptake coefficient determined on suspended particles of calcite (CaCO₃) is $1.4 (\pm 0.1) \times 10^{-4}$ and $5.5 \pm (0.1) \times 10^{-5}$ on alumina (α -Al₂O₃AlO₃).

Zogka et al. (2024) used a Knudsen cell to evaluate the initial and steady-state glyoxal uptake coefficient bulk soil samples of various origins. At low RH, these authors found that for Gobi soil sieved to less than 63 µm in diameter, the initial uptake coefficient using the geometric surface area was 0.18 (corresponding to an upper limit of the

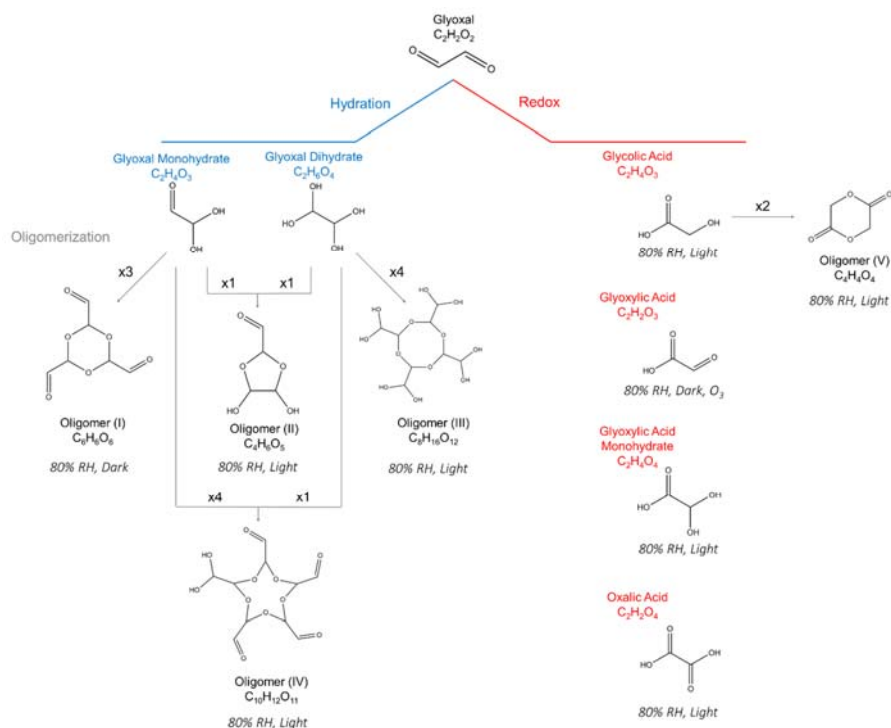
uptake), independent of glyoxal concentration. However, the steady state uptake coefficients determined after a long processing of the surface were found to decrease with increasing glyoxal concentration, due to aging of the surface.

Various reasons could induce those apparent differences. First, the differences in the experimental set up as in CESAM, the initial uptake coefficient was measured on dust aerosol particles in suspension in a large volume, compared to sieved soil (Zogka et al., 2024) and grinded mineral powders (Shen et al., 2016). The uptake coefficient is inversely proportional to the available particle surface. In our experiments, the dust available geometric surface density, calculated from the measured size distribution assuming spherical particles, is in the range $0.35\text{--}6.3 \times 10^{-3} \text{ m}^2 \text{ m}^{-3}$ (Table 2). As the CESAM chamber volume is equal to 4.2 m^3 , the total dust surface area available for the reaction ranges from 2 to $2.6 \times 10^{-3} \text{ m}^2$, several orders of magnitude lower than in the experiments designed by Shen et al. (2016) and Zogka et al. (2024). Shen et al. (2016) used model powders of various sizes between 35 nm and 5 μm , with BET (define BET) surface areas ranging between 1.4 and $440 \text{ m}^2 \text{ g}^{-1}$. In the conservative assumption that only 5 mg of the model powder was used, the total reactive surface area was up to 2.2 m^2 . Zogka et al. (2024) used the soil from Gobi sieved to 63 μm and a BET surface area of $10.5 \pm 1.0 \text{ m}^2 \text{ g}^{-1}$. Using even just 1 g would yield a surface area of the order of 10.5 m^2 . Differences in the results could also arise by differences in the dust mineralogy, which are difficult to ascertain in the present study.

Our estimated uptake coefficient of glyoxal on mineral dust is also nearly two orders of magnitude higher than for ammonium sulphate ($\gamma_{\text{gas-AS}} = 1.1 (\pm 0.2) \times 10^{-4}$; our study as well as Curry et al., 2018; De Haan et al., 2020; Galloway et al., 2009; Liggio et al., 2005b, a; Trainic et al., 2011), but lower than $\gamma_{\text{gas-AS}} = 2.9 \times 10^{-3}$ at a lower RH (Liggio et al., 2005). The difference could be due to the higher hygroscopicity of ammonium sulphate, enhancing water's competition with glyoxal for adsorption sites at 80% RH, when indeed ammonium sulphate is deliquescent. This suggests, nonetheless, that dust aerosols could play a very substantial role in the formation of organic aerosols at high RH compared to ammonium sulphate, which is often used as an aerosol proxy.

4.2. Mechanism of chemical transformation

Figure 7 illustrates the suggested chemical mechanisms of the transformation of gas-phase glyoxal on the mineral dust particles.



690

691 **Figure 7.** Proposed reaction scheme to explain the glyoxal-related molecular formulas detected through
 692 ESI-Orbitrap mass spectrometry and SFE/GC-MS.

693

694 The multiphase chemistry of glyoxal on mineral dust particles, leading to the formation
 695 of low-volatility, particle-phase products, is complex, involving hydration, redox, and
 696 oligomerization pathways. The chemical transformation of glyoxal upon uptake by
 697 mineral dust particles primarily occurs through aqueous-phase reactions. The
 698 mechanism is initiated by the hydration of glyoxal's aldehyde groups, forming mono-
 699 and di-hydrated species. These hydrated intermediates undergo condensation
 700 reactions, which involve nucleophilic attack and lead to the formation of cyclic acetal
 701 structures, particularly from two to five-membered dioxolane rings. This mechanism is
 702 well supported by prior studies (Loeffler et al., 2006; Kua et al., 2008; Hastings et al.,
 703 2005), which have described similar pathways for glyoxal oligomerization in aqueous
 704 environments.

705 This study provides new insight into this chemistry on mineral surfaces. While previous
706 research has shown that glyoxal typically forms dimers and trimers in aqueous solution
707 (Liggio et al., 2005; Nozière et al., 2009), our mass spectral data reveal the presence
708 of oligomeric species containing up to 5 glyoxal units. This higher degree of
709 oligomerization - also observed by Shen et al. (2016) - suggests that the particle-phase
710 environment allows for extended oligomer growth. The likely contributing factors
711 include reduced water activity, surface confinement, and enhanced proximity of
712 reactants, all of which promote successive addition reactions that may be hindered in
713 bulk solution (Gomez et al., 2015; Avzianova & Brooks, 2013). Concerning hydration
714 reactions, Shen et al. (2016) showed that both glyoxal and water can accumulate onto
715 dust particle surfaces (as evidenced by FTIR spectra), promoting hydration reactions
716 through surface confinement of the reagents. Absorption of water on dust surfaces can
717 also promote oligomerisation, both directly (hydration is the first step of the
718 oligomerisation reaction) as well as indirectly by enhancing particles' ability to absorb
719 glyoxal.

720 Concerning oxidation, leading to organic acid formation, the dust surface could
721 contribute directly to this mechanism by providing redox reactive sites (Shen et al.,
722 2016). Redox reactions promoted the formation of glycolic, glyoxylic, and oxalic acids.
723 These compounds not only represent aging products but also participate in further
724 condensation reactions, expanding the chemical diversity of SOA. In particular, we
725 detected the presence of oligomer V, which we propose results not from direct glyoxal
726 self-reactions but rather from the condensation of two glycolic acid molecules. This
727 suggests a broader heterogeneous transformation process occurring on the dust
728 surface, possibly involving oxidative pathways. Such cross-reactions are consistent
729 with mechanisms proposed in glyoxal–methylglyoxal systems (Zhang et al., 2022),
730 where mixed oligomers form through shared reaction intermediates.

731 A key aspect of our findings is the irreversibility of glyoxal uptake on mineral dust. In
732 contrast to bulk aqueous systems, where glyoxal oligomerization can exist in
733 equilibrium with monomeric species, our results suggest that oligomer formation on
734 mineral particles is effectively irreversible. The persistence of high-molecular-weight
735 products following drying and thermal analysis confirms that these species are
736 chemically stable and remain in the condensed phase. This behaviour is consistent

with previous observations (Hastings et al., 2005; Ortiz-Montalvo et al., 2014) and highlights the significance of particle-phase reactions in the formation of SOA.

The acidity of the particle surface could potentially play a role in catalysing glyoxal oligomerization. It is plausible that localized acidity arises or is enhanced by the accumulation of transformation products such as glycolic and oxalic acids, which were detected in this study. This in-situ acidification may facilitate acid-catalysed reaction pathways even under neutral or weakly acidic conditions. The importance of acidity in glyoxal chemistry is supported by mechanistic proposals involving carbenium ion intermediates or hydrogen-bond-assisted nucleophilic mechanisms, which can operate effectively without requiring strongly acidic environments (Zhang et al., 2022; Gomez et al., 2015). These pathways are known to promote the formation of low-volatility oligomers, contributing to organic aerosol mass. Similarly, Ortiz-Montalvo et al. (2014) demonstrated that even mildly acidic aerosols significantly enhance glyoxal oligomerization and SOA formation.

Another critical factor is the presence of adsorbed water on mineral dust particles. Our findings demonstrate, in fact, that the availability of surface water facilitates organic aerosol formation from glyoxal. This agrees with chamber and field studies (Hastings et al., 2005; Shen et al., 2016) that identified a RH threshold above which glyoxal uptake dramatically increases. The presence of a thin aqueous film on the particle surface creates a reactive medium where glyoxal can concentrate, hydrate, and polymerize efficiently. Even after evaporation, the products formed are retained in the particle phase, evidencing their low volatility and chemical resilience.

4.3. Implications for the dust properties

The irreversible transformation of the chemical composition of mineral dust following the uptake of glyoxal could influence the physico-chemical properties of mineral dust particles. The formation of organic acids (glycolic, glyoxylic and oxalic acids) should change the dust pH, increasing its acidity and ability to dissolve transition metals like iron and copper. This could alter their speciation, enhancing their bioavailability in aqueous aerosol environments and potentially impacting atmospheric chemistry and the reactivity of aerosol particles (Giorio et al., 2022). Changes in dust pH could also affect its hygroscopic properties, influencing its ability to adsorb water and grow in size. This is consistent with our observation regarding the volume increase of dust particles after the uptake and the subsequent growth that enhances particle interaction with light

770 and cloud droplets formation. Collectively, these processes highlight how aerosol
771 acidity modulates not only chemical transformations but also key physical properties
772 and atmospheric lifetimes of dust-glyoxal systems.

773 The newly formed organic matter from glyoxal on dust particles could also alter the
774 aerosol's optical properties, affecting its ability to absorb solar radiation, as recently
775 observed in aqueous solution (De Haan et al., 2023) or on ammonium sulphate
776 aerosols (De Haan et al. 2020; Trainic et al. 2011). The presence of hydrated glyoxal
777 oligomeric structures has already been observed to have UV radiation absorption
778 properties (Kalberer et al., 2004; Shapiro et al., 2009). Glyoxal-derived oligomers could
779 significantly influence the optical properties of mineral dust aerosols. Spectroscopic
780 analyses revealed that these oligomers have broadened OH and C–O bands and
781 enhanced Raman activity, indicative of their hydrated and cyclic structures (Avzianova
782 and Brooks, 2013). They also have strong UV-visible absorption, particularly between
783 300–600 nm, with characteristic shoulders at ~280 and 345 nm attributed to acetal and
784 aldol condensation products (Schwier et al., 2010; Shapiro et al., 2009). High RH
785 conditions (> 80%) facilitate brown carbon formation, evidenced by the further
786 appearance of UV-visible absorbance peaks and Raman background signals (De
787 Haan et al., 2020; Zhang et al., 2022).

788 **5. Conclusions**

789 This paper presented a novel investigation of the interaction between gas-phase
790 glyoxal and mineral dust. By taking advantage of the capabilities of the CESAM
791 atmospheric simulation chamber to perform multiphase experiments on time scales
792 relevant to atmospheric processes and dispersion, including aerosols, our experiments
793 considered airborne submicron mineral dust particles generated from a natural soil
794 (Gobi Desert) in realistic concentrations, composition and size distribution. While
795 airborne, the dust aerosol was aged under variable conditions of RH, irradiation, and
796 ozone concentrations. Our study investigates, for the first time, both the rate of uptake
797 of glyoxal and the rate of formation of the organic aerosol from the gas-phase uptake,
798 while providing the chemical composition of the organic matter formed on the dust
799 particles, and its implications on the particle microphysics.

800 This study used a single and instantaneous injection of glyoxal, and not a constant
801 steady state flux. Above 30% RH, upon injection, glyoxal is partitioned almost

802 instantaneously between the gas phase, the chamber walls and the dust particles. This
803 is an advantage to scale our results to ambient conditions. Indeed, Volkamer et al.
804 (2005) estimated that the daytime lifetime of glyoxal is around 1.3 h. Alvarado et al.
805 (2020) showed that the long-range transport of glyoxal produced from a point source
806 (e.g., Canadian wildfires) may be possible only by invoking the progressive oxidation
807 of its longer-lived precursors in the plume. In the scenario where dust aerosols interact
808 with a glyoxal plume from a point source, one can expect an interaction time of a few
809 minutes, compatible with that of this study. Furthermore, because the uptake follows a
810 first-order kinetics, the measured uptake coefficient ($\gamma = (9 \pm 5) \times 10^{-3}$ at 80% RH) is
811 independent of the glyoxal concentration and transferable to atmospheric conditions.

812 The uptake of glyoxal and the formation of organic matter start as soon as the glyoxal
813 is injected into the chamber and last approximately 20 minutes. After this time, the dust
814 surface seems saturated, likely because of the excessive glyoxal concentrations
815 injected in the chamber. On the other hand, the uptake coefficient measured by the
816 loss of gas-phase glyoxal molecules agrees very well with the rate of formation of the
817 particulate organic mass on the dust, suggesting that the totality of the mass of reacting
818 glyoxal is condensed on the dust particles. While some of the organic matter is lost
819 again from the dust particles due to evaporation, oligomers and organic acids are
820 detected on the dust even after the uptake has finished, indicating that the uptake of
821 glyoxal modifies irreversibly both the composition and the physical properties of
822 mineral dust.

823 This study reveals a significant quantitative transfer of gas-phase glyoxal molecules to
824 mineral dust aerosol surfaces, occurring within a timescale of a few minutes,
825 underscoring the important role of dust-glyoxal interactions in the atmosphere. Our
826 results extend the current understanding of glyoxal chemistry in atmospheric systems.
827 While oligomerization occurs through well-established aqueous-phase pathways, we
828 suggest that mineral dust particles facilitate, in a unique way, higher-order oligomer
829 formation, support irreversible uptake, and possibly promote alternative reaction
830 channels such as glycolic acid condensation. These findings underscore the
831 importance of mineral dust surfaces as active sites for multiphase SOA formation, with
832 implications for understanding aerosol growth, composition, and climate-relevant
833 properties. This is also in agreement with the field observations conducted by Wang et
834 al. (2015). Neglecting the uptake pathway on dust could result in an underestimation

835 of glyoxal removal from the atmosphere, potentially leading to disparities between
836 model predictions and observed gaseous concentrations of glyoxal (Kluge et al., 2023;
837 Ling et al., 2020; Volkamer et al., 2007; Washenfelder et al., 2011). The findings of this
838 study also have important implications for the aerosol direct and indirect radiative effect
839 and aerosol pH. The acidification and the oxidation of the dust aerosols by glyoxal
840 should increase their hygroscopicity, especially under high RH conditions, affecting
841 particle growth dynamics, phase behaviour, and cloud condensation nuclei (CCN)
842 potential (Song and Osada, 2021). Further data analysis is ongoing to address these
843 aspects.

844

845 **Data availability.** The simulation chamber experiments that support the findings of this study
846 are available through the Database of Atmospheric Simulation Chamber Studies (DASCS) of
847 the EUROCHAMP Data Centre ([https:// data.eurochamp.org/ data- access/ chamber-](https://data.eurochamp.org/data-access/chamber-experiments/)
848 [experiments/](https://data.eurochamp.org/data-access/chamber-experiments/)).

849 **Code availability.** The routine used for fitting the size distribution is available at
850 <https://doi.org/10.5281/zenodo.8135133> (Baldo and Lu, 2023). Note that in this study, we only
851 used the size distribution measured by the OPC instrument, which was fitted with a lognormal
852 function. The Tof-ACSM data processing (including mass calibration, peaks integration and air
853 beam correction of ion intensities) was conducted with Tofware version 3_2_40209, the ACSM
854 data analysis package for the software Igor Pro 7.08 (Wavemetrics, Inc., Portland, OR, USA).
855 SFE-GC-MS data analysis was conducted using the proprietary software (TurboMass Version
856 6.1.0.1965 PerkinElmer®).

857 **Author contributions.** PF, JFD and FB conceptualized the study. PF and FB led the paper
858 writing, with contributions from all the authors. JFD provided with expertise on multi-phase
859 chemistry. CB analysed the aerosol size distribution data. VM supervised the analysis of PTR-
860 MS data. FB, CG and DLP performed the ESI-Orbitrap analysis of filter samples. FB and JFB
861 performed the analysis of ACSM observations. FB, TB and AG performed the SFE/CG-MS
862 analysis of filter samples. FB, GN and SC performed the thermo-optical analysis of filter
863 samples. FB, MC, AB, EP, VM, BPV and PF conducted the chamber experiments. MR
864 provided with the soil sample and expertise on heterogeneous chemistry. PF provided with
865 funding.

866 **Competing interests.** The authors declare no competing interests.

867 **Special issue statement.** This article is not part of a special issue. It is not associated with a
868 conference.

869 **Acknowledgements.** The AERIS data center (www.aeris-data.fr) is acknowledged for
870 distributing and curing the data produced by the CESAM chamber through the hosting of the
871 EUROCHAMP data center (<https://data.eurochamp.org>). The initial contribution of M. Giordano
872 (Afri-SET) to the conceptualisation of the project is gratefully acknowledged. The authors wish
873 to thank the two anonymous referees for helping to improve the manuscript.

874 **Financial support.** This work has received funding from the French National Research
875 Agency (ANR) through the research project CLIMDO under the grant number ANR-19-CE01-
876 0008-02. It has received support from the European Union's Horizon 2020 research and
877 innovation program through the EUROCHAMP-2020 Infrastructure Activity under grant
878 agreement no. 730997. CNRS-INSU is gratefully acknowledged for supporting the CESAM
879 chamber as a national facility as part of the French ACTRIS Research Infrastructure. ESI-

880 Orbitrap analyses was supported by a BP next generation fellowship awarded by the Yusuf
881 Hamied Department of Chemistry at the University of Cambridge to CG.

References

- Adebiyi, A., Kok, J. F., Murray, B. J., Ryder, C. L., Stuut, J.-B. W., Kahn, R. A., Knippertz, P., Formenti, P., Mahowald, N. M., Pérez García-Pando, C., Klose, M., Ansmann, A., Samset, B. H., Ito, A., Balkanski, Y., Di Biagio, C., Romanias, M. N., Huang, Y., and Meng, J.: A review of coarse mineral dust in the Earth system, *Aeolian Research*, 60, 100849, <https://doi.org/10.1016/j.aeolia.2022.100849>, 2023.
- Aiken, A. C., DeCarlo, P. F., Kroll, J. H., Worsnop, D. R., Huffman, J. A., Docherty, K. S., Ulbrich, I. M., Mohr, C., Kimmel, J. R., Sueper, D., Sun, Y., Zhang, Q., Trimborn, A., Northway, M., Ziemann, P. J., Canagaratna, M. R., Onasch, T. B., Alfarra, M. R., Prevot, A. S. H., Dommen, J., Duplissy, J., Metzger, A., Baltensperger, U., and Jimenez, J. L.: O/C and OM/OC Ratios of Primary, Secondary, and Ambient Organic Aerosols with High-Resolution Time-of-Flight Aerosol Mass Spectrometry, *Environ. Sci. Technol.*, 42, 4478–4485, <https://doi.org/10.1021/es703009q>, 2008.
- Alvarado, L. M. A., Richter, A., Vrekoussis, M., Hilboll, A., Kalisz Hedegaard, A. B., Schneising, O., and Burrows, J. P.: Unexpected long-range transport of glyoxal and formaldehyde observed from the Copernicus Sentinel-5 Precursor satellite during the 2018 Canadian wildfires, *Atmos. Chem. Phys.*, 20, 2057–2072, <https://doi.org/10.5194/acp-20-2057-2020>, 2020.
- Atkinson, J. D., Murray, B. J., Woodhouse, M. T., Whale, T. F., Baustian, K. J., Carslaw, K. S., Dobbie, S., O'Sullivan, D., and Malkin, T. L.: The importance of feldspar for ice nucleation by mineral dust in mixed-phase clouds, *Nature*, 498, 355–358, <https://doi.org/10.1038/nature12278>, 2013.
- Avzianova, E., and Brooks, S. D.: Raman spectroscopy of glyoxal oligomers in aqueous solutions, *Spectrochimica Acta Part A: Molecular and Biomolecular Spectroscopy*, 101, 40–48, <https://doi.org/10.1016/j.saa.2012.09.050>, 2013.
- Baldo, C., Formenti, P., Di Biagio, C., Lu, G., Song, C., Cazaunau, M., Pangui, E., Doussin, J.-F., Dagsson-Waldhauserova, P., Arnalds, O., Beddows, D., MacKenzie, A. R., and Shi, Z.: Complex refractive index and single scattering albedo of Icelandic dust in the shortwave part of the spectrum, *Atmos. Chem. Phys.*, 23, 7975–8000, <https://doi.org/10.5194/acp-23-7975-2023>, 2023.
- Battaglia, F., Baldo, C., Cazaunau, M., Bergé, A., Pangui, E., Picquet-Varrault, B., Doussin, J.-F., and Formenti, P.: Protocol for generating realistic submicron mono-dispersed mineral dust particles in simulation chambers and laboratory experiments, *Aerosol Science and Technology*, 59, 357–369, <https://doi.org/10.1080/02786826.2024.2442518>, 2025.
- Bauer, S. E., Mishchenko, M. I., Lacis, A. A., Zhang, S., Perlwitz, J., and Metzger, S. M.: Do sulfate and nitrate coatings on mineral dust have important effects on radiative properties and climate modeling?, *J. Geophys. Res.*, 112, D06307, <https://doi.org/10.1029/2005JD006977>, 2007.
- Brégonzio-Rozier, L., Giorio, C., Siekmann, F., Pangui, E., Morales, S. B., Temime-Roussel, B., Gratien, A., Michoud, V., Cazaunau, M., DeWitt, H. L., Tapparo, A., Monod, A., and Doussin, J.-F.: Secondary organic aerosol formation from isoprene photooxidation during cloud condensation–evaporation cycles, *Atmos. Chem. Phys.*, 16, 1747–1760, <https://doi.org/10.5194/acp-16-1747-2016>, 2016.
- Buxton, G. V., Malone, T. N., and ~~G.~~ Arthur Salmon, ~~G.~~: Oxidation of glyoxal initiated by OH in oxygenated aqueous solution, *Faraday Trans.*, 93, 2889–2891, <https://doi.org/10.1039/a701468f>, 1997.
- Carlton, A. G., Turpin, B. J., Altieri, K. E., Seitzinger, S., Reff, A., Lim, H.-J., and Ervens, B.: Atmospheric oxalic acid and SOA production from glyoxal: Results of aqueous photooxidation experiments, *Atmospheric — Atmos. Environment Environ.*, 41, 7588–7602, <https://doi.org/10.1016/j.atmosenv.2007.05.035>, 2007.
- Castellanos, P., Colarco, P., Espinosa, W. R., Guzewich, S. D., Levy, R. C., Miller, R. L., Chin, M., Kahn, R. A., Kemppinen, O., Moosmüller, H., Nowotnick, E. P., Rocha-Lima, A., Smith, M. D., Yorks, J. E., and Yu, H.: Mineral dust optical properties for remote sensing and global modeling: A review, *Remote — Rem. Sensing of Environment Environ.*, 303, 113982, <https://doi.org/10.1016/j.rse.2023.113982>, 2024.

- 933 Chan, C., Jacob, D. J., Marais, E. A., Yu, K., Travis, K. R., Kim, P. S., Fisher, J. A., Zhu, L., Wolfe, G.
934 M., Hanisco, T. F., Keutsch, F. N., Kaiser, J., Min, K.-E., Brown, S. S., Washenfelder, R. A.,
935 González Abad, G., and Chance, K.: Glyoxal yield from isoprene oxidation and relation to
936 formaldehyde: chemical mechanism, constraints from SENEX aircraft observations, and
937 interpretation of OMI satellite data, *Atmos. Chem. Phys.*, 17, 8725–8738,
938 <https://doi.org/10.5194/acp-17-8725-2017>, 2017.
- 939 Chen, S., Chen, J., Zhang, Y., Lin, J., Bi, H., Song, H., Chen, Y., Lian, L., Liu, C., and Zhang, R.:
940 Anthropogenic dust: sources, characteristics and emissions, *Environ. Res. Lett.*, 18, 103002,
941 <https://doi.org/10.1088/1748-9326/acf479>, 2023.
- 942 Chirizzi, D., Cesari, D., Guascito, M. R., Dinoi, A., Giotta, L., Donato, A., and Contini, D.: Influence of
943 Saharan dust outbreaks and carbon content on oxidative potential of water-soluble fractions of
944 PM_{2.5} and PM₁₀. *Atmos. Environ.*, 163, 1–8, <https://doi.org/10.1016/j.atmosenv.2017.05.021>.
945 2017. Chirizzi, D.: Influence of Saharan dust outbreaks and carbon content on oxidative potential
946 of water-soluble fractions of PM_{2.5} and PM₁₀. *Atmospheric Environment*, 2017.
- 947 Crowley, J. N., Ammann, M., Cox, R. A., Hynes, R. G., Jenkin, M. E., Mellouki, A., Rossi, M. J., Troe,
948 J., and Wallington, T. J.: Evaluated kinetic and photochemical data for atmospheric chemistry:
949 Volume V – heterogeneous reactions on solid substrates, *Atmos. Chem. Phys.*, 10, 9059–9223,
950 <https://doi.org/10.5194/acp-10-9059-2010>, 2010.
- 951 De Haan, D. O., Hawkins, L. N., Jansen, K., Welsh, H. G., Pednekar, R., De Loera, A., Jimenez, N. G.,
952 Tolbert, M. A., Cazaunau, M., Gratien, A., Bergé, A., Pangui, E., Formenti, P., and Doussin, J.-
953 F.: Glyoxal's impact on dry ammonium salts: fast and reversible surface aerosol browning, *Atmos.*
954 *Chem. Phys.*, 20, 9581–9590, <https://doi.org/10.5194/acp-20-9581-2020>, 2020.
- 955 De Haan, D. O., Hawkins, L. N., Wickremasinghe, P. D., Andretta, A. D., Dignum, J. R., De Haan, A. C.,
956 Welsh, H. G., Pennington, E. A., Cui, T., Surratt, J. D., Cazaunau, M., Pangui, E., and Doussin,
957 J.-F.: Brown Carbon from Photo-Oxidation of Glyoxal and SO₂ in Aqueous Aerosol, *ACS Earth*
958 *Space Chem.*, 7, 1131–1140, <https://doi.org/10.1021/acsearthspacechem.3c00035>, 2023.
- 959 Denjean, C., Formenti, P., Picquet-Varraut, B., Katrib, Y., Pangui, E., Zapf, P., and Doussin, J. F.: A
960 new experimental approach to study the hygroscopic and optical properties of aerosols:
961 application to ammonium sulfate particles, *Atmos. Meas. Tech.*, 7, 183–197,
962 <https://doi.org/10.5194/amt-7-183-2014>, 2014.
- 963 Di Biagio, C., Formenti, P., Balkanski, Y., Caponi, L., Cazaunau, M., Pangui, E., Journet, E., Nowak, S.,
964 Caquineau, S., Andreae, M. O., Kandler, K., Saeed, T., Piketh, S., Seibert, D., Williams, E., and
965 Doussin, J.-F.: Global scale variability of the mineral dust long-wave refractive index: a new
966 dataset of in situ measurements for climate modeling and remote sensing, *Atmos. Chem. Phys.*,
967 17, 1901–1929, <https://doi.org/10.5194/acp-17-1901-2017>, 2017.
- 968 Di Biagio, C., Formenti, P., Balkanski, Y., Caponi, L., Cazaunau, M., Pangui, E., Journet, E., Nowak, S.,
969 Andreae, M. O., Kandler, K., Saeed, T., Piketh, S., Seibert, D., Williams, E., and Doussin, J.-F.:
970 Complex refractive indices and single-scattering albedo of global dust aerosols in the shortwave
971 spectrum and relationship to size and iron content, *Atmos. Chem. Phys.*, 19, 15503–15531,
972 <https://doi.org/10.5194/acp-19-15503-2019>, 2019.
- 973 Dupart, Y., King, S. M., Nekat, B., Nowak, A., Wiedensohler, A., Herrmann, H., David, G., Thomas, B.,
974 Miffre, A., Rairoux, P., D'Anna, B., and George, C.: Mineral dust photochemistry induces
975 nucleation events in the presence of SO₂, *Proc. Natl. Acad. Sci. U.S.A.*, 109, 20842–20847,
976 <https://doi.org/10.1073/pnas.1212297109>, 2012.
- 977 Ervens, B. and Volkamer, R.: Glyoxal processing by aerosol multiphase chemistry: towards a kinetic
978 modeling framework of secondary organic aerosol formation in aqueous particles, *Atmos. Chem.*
979 *Phys.*, 10, 8219–8244, <https://doi.org/10.5194/acp-10-8219-2010>, 2010.
- 980 Fröhlich, R., Cubison, M. J., Slowik, J. G., Bukowiecki, N., Prévôt, A. S. H., Baltensperger, U., Schneider,
981 J., Kimmel, J. R., Gonin, M., Rohner, U., Worsnop, D. R., and Jayne, J. T.: The ToF-ACSM: a
982 portable aerosol chemical speciation monitor with TOFMS detection, *Atmos. Meas. Tech.*, 6,
983 3225–3241, <https://doi.org/10.5194/amt-6-3225-2013>, 2013.

Mis en forme : Police :10 pt, Anglais (États-Unis)

Mis en forme : Police :10 pt, Anglais (États-Unis)

Mis en forme : Police :10 pt, Anglais (États-Unis)

Mis en forme : Indice

Mis en forme : Indice

984 Fu, T.-M., Jacob, D. J., Wittrock, F., Burrows, J. P., Vrekoussis, M., and Henze, D. K.: Global budgets
 985 of atmospheric glyoxal and methylglyoxal, and implications for formation of secondary organic
 986 aerosols, *J. Geophys. Res.*, 113, D15303, <https://doi.org/10.1029/2007JD009505>, 2008.

987 ~~Galloway, M. M., Chhabra, P. S., Chan, A. W. H., Surratt, J. D., Flagan, R. C., Seinfeld, J. H., and~~
 988 ~~Keutsch, F. N.: Glyoxal uptake on ammonium sulphate seed aerosol: reaction products and~~
 989 ~~reversibility of uptake under dark and irradiated conditions, *Atmos. Chem. Phys.*, 9, 3331–3345,~~
 990 ~~<https://doi.org/10.5194/acp-9-3331-2009>, 2009.~~

991 ~~Galloway, M. M., Chhabra, P. S., Chan, A. W. H., Surratt, J. D., Flagan, R. C., Seinfeld, J. H., and~~
 992 ~~Keutsch, F. N.: Glyoxal uptake on ammonium sulphate seed aerosol: reaction products and~~
 993 ~~reversibility of uptake under dark and irradiated conditions, *Atmos. Chem. Phys.*, 2009.~~

994 Giorio, C., Monod, A., Brégonzio-Rozier, L., DeWitt, H. L., Cazaunau, M., Temime-Roussel, B., Gratien,
 995 A., Michoud, V., Pangu, E., Ravier, S., Zielinski, A. T., Tapparo, A., Vermeylen, R., Claeys, M.,
 996 Voisin, D., Kalberer, M., and Doussin, J.-F.: Cloud Processing of Secondary Organic Aerosol from
 997 Isoprene and Methacrolein Photooxidation, *J. Phys. Chem. A*, 121, 7641–7654,
 998 <https://doi.org/10.1021/acs.jpca.7b05933>, 2017.

999 Giorio, C., D'Aronco, S., Di Marco, V., Badocco, D., Battaglia, F., Soldà, L., Pastore, P., and Tapparo,
 1000 A.: Emerging investigator series: aqueous-phase processing of atmospheric aerosol influences
 1001 dissolution kinetics of metal ions in an urban background site in the Po Valley, *Environ. Sci.:*
 1002 *Processes* Impacts, 24, 884–897, <https://doi.org/10.1039/D2EM00023G>, 2022.

1003 Gomez, M. E., Lin, Y., Guo, S., & Zhang, R. (2015). Heterogeneous Chemistry of Glyoxal on Acidic
 1004 Solutions. An Oligomerization Pathway for Secondary Organic Aerosol Formation. ~~The Journal~~
 1005 ~~of, *Physical Phys. Chem*~~*Chemistry A*, 119(19), 4457–4463. <https://doi.org/10.1021/jp509916r>

1006 Goodman, A. L., Underwood, G. M., and Grassian, V. H.: Heterogeneous Reaction of NO₂:
 1007 Characterization of Gas-Phase and Adsorbed Products from the Reaction, 2NO₂(g) + H₂O(a)
 1008 → HONO(g) + HNO₃(a) on Hydrated Silica Particles, *J. Phys. Chem. A*, 103, 7217–7223,
 1009 <https://doi.org/10.1021/jp9910688>, 1999.

1010 Guo, Y., Wang, S., Zhu, J., Zhang, R., Gao, S., Saiz-Lopez, A., and Zhou, B.: Atmospheric
 1011 formaldehyde, glyoxal and their relations to ozone pollution under low- and high-NO_x regimes in
 1012 summertime Shanghai, China, ~~Atmospheric~~ *Atmos. Research*, 258, 105635,
 1013 <https://doi.org/10.1016/j.atmosres.2021.105635>, 2021.

1014 Harrison, S. P., Kohfeld, K. E., Roelandt, C., and Claquin, T.: The role of dust in climate changes today,
 1015 at the last glacial maximum and in the future, *Earth-Science Reviews*, 54, 43–80,
 1016 [https://doi.org/10.1016/S0012-8252\(01\)00041-1](https://doi.org/10.1016/S0012-8252(01)00041-1), 2001.

1017 ~~Hastings, W. P., Koehler, C. A., Bailey, E. L., and De Haan, D. O.: (2005)-Secondary Organic Aerosol~~
 1018 ~~Formation by Glyoxal Hydration and Oligomer Formation: Humidity Effects and Equilibrium Shifts~~
 1019 ~~during Analysis. *Environmental Environ. Science & Technology*~~*Techn.*, 39(22), 8728–8735.
 1020 ~~<https://doi.org/10.1021/es050446l>, 2005~~

1021 ~~Hettiarachchi, E., and Grassian, V. H.: Heterogeneous Reactions of Phenol on Different Components of~~
 1022 ~~Mineral Dust Aerosol: Formation of Oxidized Organic and Nitro-Phenolic Compounds, *ACS ES&T*~~
 1023 ~~*Air*, 1, 259–272, 10.1021/acsestair.3c00042, 2024.~~

1024 ~~Hettiarachchi, E., and Grassian, V. H.: Heterogeneous Reactions of Phenol on Different Components of~~
 1025 ~~Mineral Dust Aerosol: Formation of Oxidized Organic and Nitro-Phenolic Compounds, *ACS EST*~~
 1026 ~~*Air*, 1, 259–272, <https://doi.org/10.1021/acsestair.3c00042>, 2024.~~

1027 ~~Horowitz, A., Meller, R., and Moortgat, G. K.: The UV–VIS absorption cross sections of the α-dicarbonyl~~
 1028 ~~compounds: pyruvic acid, biacetyl and glyoxal, *J. Photochem. Photobiol. A: Chemistry*, 146, 19–~~
 1029 ~~27, [https://doi.org/10.1016/S1010-6030\(01\)00601-3](https://doi.org/10.1016/S1010-6030(01)00601-3), 2001.~~

1030 ~~Horowitz, A., Meller, R., and Moortgat, G. K.: The UV–VIS absorption cross sections of the α-dicarbonyl~~
 1031 ~~compounds: pyruvic acid, biacetyl and glyoxal, 2001.~~

1032 Hu, J., Chen, Z., Qin, X., and Dong, P.: Reversible and irreversible gas–particle partitioning of dicarbonyl
1033 compounds observed in the real atmosphere, *Atmos. Chem. Phys.*, 22, 6971–6987,
1034 <https://doi.org/10.5194/acp-22-6971-2022>, 2022.

1035 Joshi, N., Romanias, M. N., Riffault, V., and Thevenet, F.: Investigating water adsorption onto natural
1036 mineral dust particles: Linking DRIFTS experiments and BET theory, *Aeolian–Aeol.
1037 ResearchRes.*, 27, 35–45, <https://doi.org/10.1016/j.aeolia.2017.06.001>, 2017.

1038 Lai, A. C. and Nazaroff, W. W.: ~~MODELING Modelling indoor particle deposition from turbulent flow onto~~
1039 ~~smooth surfacesINDOOR PARTICLE DEPOSITION FROM TURBULENT FLOW ONTO~~
1040 ~~SMOOTH SURFACES~~, *Journal of J. Aerosol–Aeros. ScienceSci.*, 31, 463–476,
1041 [https://doi.org/10.1016/S0021-8502\(99\)00536-4](https://doi.org/10.1016/S0021-8502(99)00536-4), 2000.

1042 Kalberer, M., Paulsen, D., Sax, M., Steinbacher, M., Dommen, J., Prevot, A. S. H., Fisseha, R.,
1043 Weingartner, E., Frankevich, V., Zenobi, R., and Baltensperger, U.: Identification of Polymers as
1044 Major Components of Atmospheric Organic Aerosols, *Science*, 303, 1659–1662,
1045 <https://doi.org/10.1126/science.1092185>, 2004.

1046 Kluge, F., Hüneke, T., Lerot, C., Rosanka, S., Rotermund, M. K., Taraborrelli, D., Weyland, B., and
1047 Pfeilsticker, K.: Airborne glyoxal measurements in the marine and continental atmosphere:
1048 comparison with TROPOMI observations and EMAC simulations, *Atmos. Chem. Phys.*, 23, 1369–
1049 1401, <https://doi.org/10.5194/acp-23-1369-2023>, 2023.

1050 Knippertz, P. and Stuut, J.-B. W. (Eds.): *Mineral Dust: A Key Player in the Earth System*, Springer
1051 Netherlands, Dordrecht, <https://doi.org/10.1007/978-94-017-8978-3>, 2014.

1052 Knote, C., Hodzic, A., Jimenez, J. L., Volkamer, R., Orlando, J. J., Baidar, S., Brioude, J., Fast, J.,
1053 Gentner, D. R., Goldstein, A. H., Hayes, P. L., Knighton, W. B., Oetjen, H., Setyan, A., Stark, H.,
1054 Thalman, R., Tyndall, G., Washenfelder, R., Waxman, E., and Zhang, Q.: Simulation of semi-
1055 explicit mechanisms of SOA formation from glyoxal in aerosol in a 3-D model, *Atmos. Chem.*
1056 *Phys.*, 14, 6213–6239, <https://doi.org/10.5194/acp-14-6213-2014>, 2014.

1057 Kok, J. F., Adebisi, A. A., Albani, S., Balkanski, Y., Checa-Garcia, R., Chin, M., Colarco, P. R., Hamilton,
1058 D. S., Huang, Y., Ito, A., Klose, M., Li, L., Mahowald, N. M., Miller, R. L., Obiso, V., Pérez García-
1059 Pando, C., Rocha-Lima, A., and Wan, J. S.: Contribution of the world's main dust source regions
1060 to the global cycle of desert dust, *Aerosols/Atmospheric Modelling/Troposphere/Physics (physical*
1061 *properties and processes)*, <https://doi.org/10.5194/acp-2021-4>, 2021.

1062 Kok, J. F., Storelvmo, T., Karydis, V. A., Adebisi, A. A., Mahowald, N. M., Evan, A. T., He, C., and Leung,
1063 D. M.: Mineral dust aerosol impacts on global climate and climate change, *Nat Rev Earth Environ*,
1064 4, 71–86, <https://doi.org/10.1038/s43017-022-00379-5>, 2023.

1065 Kourtchev, I., Doussin, J.-F., Giorio, C., Mahon, B., Wilson, E. M., Maurin, N., Pangui, E., Venables, D.
1066 S., Wenger, J. C., and Kalberer, M.: Molecular composition of fresh and aged secondary organic
1067 aerosol from a mixture of biogenic volatile compounds: a high-resolution mass spectrometry
1068 study, *Atmos. Chem. Phys.*, 15, 5683–5695, <https://doi.org/10.5194/acp-15-5683-2015>, 2015.

1069 Kroll, J. H., Ng, N. L., Murphy, S. M., Varutbangkul, V., Flagan, R. C., and Seinfeld, J. H.: Chamber
1070 studies of secondary organic aerosol growth by reactive uptake of simple carbonyl compounds,
1071 *J. Geophys. Res.*, 110, 2005JD006004, <https://doi.org/10.1029/2005JD006004>, 2005.

1072 Kua, J., Hanley, S. W., ~~and~~ De Haan, D. O. (2008). Thermodynamics and Kinetics of Glyoxal Dimer
1073 Formation: A Computational Study, *The Journal of Physical-Phys. Chemistry–Chem.* A, 112(1),
1074 66–72. <https://doi.org/10.1021/jp076573g>

1075 Lewis, A. C., Hopkins, J. R., Carslaw, D. C., Hamilton, J. F., Nelson, B. S., Stewart, G., Dernie, J.,
1076 Passant, N., and Murrells, T.: An increasing role for solvent emissions and implications for future
1077 measurements of volatile organic compounds, *Phil. Trans. R. Soc. A.*, 378, 20190328,
1078 <https://doi.org/10.1098/rsta.2019.0328>, 2020.

1079 Li, G., Cheng, Y., Kuhn, U., Xu, R., Yang, Y., Meusel, H., Wang, Z., Ma, N., Wu, Y., Li, M., Williams, J.,
1080 Hoffmann, T., Ammann, M., Pöschl, U., Shao, M., and Su, H.: Physicochemical uptake and
1081 release of volatile organic compounds by soil in coated-wall flow tube experiments with ambient
1082 air, *Atmos. Chem. Phys.*, 19, 2209–2232, <https://doi.org/10.5194/acp-19-2209-2019>, 2019.

Li, L., Mahowald, N. M., Miller, R. L., Pérez García-Pando, C., Klose, M., Hamilton, D. S., Gonçalves Ageitos, M., Ginoux, P., Balkanski, Y., Green, R. O., Kalashnikova, O., Kok, J. F., Obiso, V., Paynter, D., and Thompson, D. R.: Quantifying the range of the dust direct radiative effect due to source mineralogy uncertainty, *Atmos. Chem. Phys.*, 21, 3973–4005, <https://doi.org/10.5194/acp-21-3973-2021>, 2021.

Li, Q., Gong, D., Wang, H., Wang, Y., Han, S., Wu, G., Deng, S., Yu, P., Wang, W., and Wang, B.: Rapid increase in atmospheric glyoxal and methylglyoxal concentrations in Lhasa, Tibetan Plateau: Potential sources and implications, *Science of The Total Environment*, 824, 153782, <https://doi.org/10.1016/j.scitotenv.2022.153782>, 2022.

Liggio, J.: Reactive uptake of glyoxal by particulate matter, *J. Geophys. Res.*, 110, D10304, <https://doi.org/10.1029/2004JD005113>, 2005a.

Liggio, J., Li, S.-M., and McLaren, R.: Heterogeneous Reactions of Glyoxal on Particulate Matter: Identification of Acetals and Sulfate Esters, *Environ. Sci. Technol.*, 39, 1532–1541, <https://doi.org/10.1021/es048375y>, 2005b.

Lim, Y. B., Tan, Y., Perri, M. J., Seitzinger, S. P., and Turpin, B. J.: Aqueous chemistry and its role in secondary organic aerosol (SOA) formation, *Atmos. Chem. Phys.*, 10, 10521–10539, <https://doi.org/10.5194/acp-10-10521-2010>, 2010.

Ling, Z., Xie, Q., Shao, M., Wang, Z., Wang, T., Guo, H., and Wang, X.: Formation and sink of glyoxal and methylglyoxal in a polluted subtropical environment: observation-based photochemical analysis and impact evaluation, *Atmos. Chem. Phys.*, 20, 11451–11467, <https://doi.org/10.5194/acp-20-11451-2020>, 2020.

Liu, C., Chu, B., Liu, Y., Ma, Q., Ma, J., He, H., Li, J., and Hao, J.: Effect of mineral dust on secondary organic aerosol yield and aerosol size in α -pinene/NO_x photo-oxidation, *Atmospheric Environment*, 77, 781–789, <https://doi.org/10.1016/j.atmosenv.2013.05.064>, 2013.

Loeffler, K. W., Koehler, C. A., Paul, N. M., & De Haan, D. O.: (2006). Oligomer Formation in Evaporating Aqueous Glyoxal and Methyl Glyoxal Solutions, *Environmental Science & Technology*, 40(20), 6318–6323. <https://doi.org/10.1021/es060810w>, 2006.

Mahowald, N., Albani, S., Kok, J. F., Engelstaeder, S., Scanza, R., Ward, D. S., and Flanner, M. G.: The size distribution of desert dust aerosols and its impact on the Earth system, *Aeolian Research*, 15, 53–71, <https://doi.org/10.1016/j.aeolia.2013.09.002>, 2014.

Ng, N. L., Canagaratna, M. R., Jimenez, J. L., Chhabra, P. S., Seinfeld, J. H., and Worsnop, D. R.: Changes in organic aerosol composition with aging inferred from aerosol mass spectra, *Atmos. Chem. Phys.*, 11, 6465–6474, <https://doi.org/10.5194/acp-11-6465-2011>, 2011.

Nie, W., Ding, A., Wang, T., Kerminen, V.-M., George, C., Xue, L., Wang, W., Zhang, Q., Petäjä, T., Qi, X., Gao, X., Wang, X., Yang, X., Fu, C., and Kulmala, M.: Polluted dust promotes new particle formation and growth, *Sci Rep*, 4, 6634, <https://doi.org/10.1038/srep06634>, 2014.

Nieder, R., Benbi, D. K., and Reichl, F. X.: Soil-Borne Particles and Their Impact on Environment and Human Health, in: *Soil Components and Human Health*, Springer Netherlands, Dordrecht, 99–177, https://doi.org/10.1007/978-94-024-1222-2_3, 2018.

Nozière, B., Dziedzic, P., and Córdova, A.: Products and Kinetics of the Liquid-Phase Reaction of Glyoxal Catalyzed by Ammonium Ions (NH₄⁺), *J. Phys. Chem. A*, 113, 231–237, <https://doi.org/10.1021/jp8078293>, 2009.

Ooki, A. and Uematsu, M.: Chemical interactions between mineral dust particles and acid gases during Asian dust events, *J. Geophys. Res.*, 110, 2004JD004737, <https://doi.org/10.1029/2004JD004737>, 2005.

Ortiz-Montalvo, D. L., Häkkinen, S. A. K., Schwier, A. N., Lim, Y. B., McNeill, V. F., and Turpin, B. J.: Ammonium Addition (and Aerosol pH) Has a Dramatic Impact on the Volatility and Yield of Glyoxal Secondary Organic Aerosol, *Environ. Sci. Technol.*, 48, 255–262, <https://doi.org/10.1021/es4035667>, 2014.

- 1132 Ponczek, M., Hayeck, N., Emmelin, C., and George, C.: Heterogeneous photochemistry of dicarboxylic
1133 acids on mineral dust, *Atmospheric Environment*, 212, 262–271,
1134 <https://doi.org/10.1016/j.atmosenv.2019.05.032>, 2019.
- 1135 Romanias, M. N., El Zein, A., and Bedjanian, Y.: Heterogeneous Interaction of H₂O₂ with TiO₂
1136 Surface under Dark and UV Light Irradiation Conditions, *J. Phys. Chem. A*, 116, 8191–8200,
1137 <https://doi.org/10.1021/jp305366v>, 2012.
- 1138 Romanias, Manolis M. N., Habib-Ourrad, H., Frédéric-Thévenet, F., and Véronique V. Riffault : -2016-
1139 "Investigating the Heterogeneous Interaction of VOCs with Natural Atmospheric Particles:
1140 Adsorption of Limonene and Toluene on Saharan Mineral Dusts.," *J. Phys. Chem. The Journal
1141 of Physical Chemistry A* 120(8):1197–1212. doi: 10.1021/acs.jpca.5b10323, 2016.-
- 1142 Rossignol, S., Aregahegn, K. Z., Tinel, L., Fine, L., Nozière, B., and George, C.: Glyoxal Induced
1143 Atmospheric Photosensitized Chemistry Leading to Organic Aerosol Growth, *Environ. Sci.
1144 Technol.*, 48, 3218–3227, <https://doi.org/10.1021/es405581g>, 2014.
- 1145 Rubasinghege, G., Ogden, S., Baltrusaitis, J., and Grassian, V. H.: Heterogeneous Uptake and
1146 Adsorption of Gas-Phase Formic Acid on Oxide and Clay Particle Surfaces: The Roles of Surface
1147 Hydroxyl Groups and Adsorbed Water in Formic Acid Adsorption and the Impact of Formic Acid
1148 Adsorption on Water Uptake, *J. Phys. Chem. A*, 117, 11316–11327,
1149 <https://doi.org/10.1021/jp408169w>, 2013.
- 1150 Safi Shalamzari, M., Ryabtsova, O., Kahnt, A., Vermeylen, R., Hérent, M., Quetin-Leclercq, J., Van Der
1151 Veken, P., Maenhaut, W., and Claeys, M.: Mass spectrometric characterization of organosulfates
1152 related to secondary organic aerosol from isoprene, *Rapid Comm Mass Spectrometry*, 27, 784–
1153 794, <https://doi.org/10.1002/rcm.6511>, 2013.
- 1154 Schwier, A. N., Sareen, N., Mitroo, D., Shapiro, E. L., and McNeill, V. F.: Glyoxal-Methylglyoxal Cross-
1155 Reactions in Secondary Organic Aerosol Formation, *Environ. Sci. Technol.*, 44, 6174–6182,
1156 <https://doi.org/10.1021/es101225q>, 2010.
- 1157 Seisel, S., Lian, Y., Keil, T., Trukhin, M. E., and Zellner, R.: Kinetics of the interaction of water vapour
1158 with mineral dust and soot surfaces at T = 298 K, *Phys. Chem. Chem. Phys.*, 6, 1926–1932,
1159 <https://doi.org/10.1039/B314568A>, 2004.
- 1160 Shapiro, E. L., Szprengiel, J., Sareen, N., Jen, C. N., Giordano, M. R., and McNeill, V. F.: Light-absorbing
1161 secondary organic material formed by glyoxal in aqueous aerosol mimics, *Atmos. Chem. Phys.*,
1162 9, 2289–2300, <https://doi.org/10.5194/acp-9-2289-2009>, 2009.
- 1163 Shapiro, E. L., Szprengiel, J., Sareen, N., Jen, C. N., Giordano, M. R., and McNeill, V. F.: Light-absorbing
1164 secondary organic material formed by glyoxal in aqueous aerosol mimics, *Atmos. Chem. Phys.*,
1165 2009.
- 1166 Shen, X., Wu, H., Zhao, Y., Huang, D., Huang, L., and Chen, Z.: Heterogeneous reactions of glyoxal on
1167 mineral particles: A new avenue for oligomers and organosulfate formation, *Atmospheric Atmos.*
1168 *Environment Environ.*, 131, 133–140, <https://doi.org/10.1016/j.atmosenv.2016.01.048>, 2016.
- 1169 Shrivastava, M., Cappa, C. D., Fan, J., Goldstein, A. H., Guenther, A. B., Jimenez, J. L., Kuang, C.,
1170 Laskin, A., Martin, S. T., Ng, N. L., Petaja, T., Pierce, J. R., Rasch, P. J., Roldin, P., Seinfeld, J.
1171 H., Shilling, J., Smith, J. N., Thornton, J. A., Volkamer, R., Wang, J., Worsnop, D. R., Zaveri, R.
1172 A., Zelenyuk, A., and Zhang, Q.: Recent advances in understanding secondary organic aerosol:
1173 Implications for global climate forcing, *Reviews of Geophysics Geophys.*, 55, 509–559,
1174 <https://doi.org/10.1002/2016RG000540>, 2017.
- 1175 Song, Q. and Osada, K.: Direct measurement of aerosol acidity using pH testing paper and hygroscopic
1176 equilibrium under high relative humidity, *Atmos. Environ. Atmospheric Environment*, 261, 118605,
1177 <https://doi.org/10.1016/j.atmosenv.2021.118605>, 2021.
- 1178 Steinke, I., Funk, R., Busse, J., Iturri, A., Kirchen, S., Leue, M., Möhler, O., Schwartz, T., Schnaiter, M.,
1179 Sierau, B., Toprak, E., Ullrich, R., Ulrich, A., Hoose, C., and Leisner, T.: Ice nucleation activity of
1180 agricultural soil dust aerosols from Mongolia, Argentina, and Germany, *J. Geophys. Res.*, 121,
1181 13559–13576, doi:10.1002/2016JD025160, 2016. JGR Atmospheres, 121,
1182 <https://doi.org/10.1002/2016JD025160>, 2016.

Mis en forme : Police :(Par défaut) Arial, 10 pt, Non Italique, Anglais (États-Unis)

Mis en forme : Police :(Par défaut) Arial, 10 pt, Anglais (États-Unis)

Mis en forme : Police par défaut, Police :(Par défaut) Arial, 10 pt, Anglais (États-Unis)

Mis en forme : Police :(Par défaut) Arial, 10 pt, Anglais (États-Unis)

Mis en forme : Police par défaut, Police :(Par défaut) Arial, 10 pt, Anglais (États-Unis)

Mis en forme : Police :(Par défaut) Arial, 10 pt, Anglais (États-Unis)

Mis en forme : Police par défaut, Police :(Par défaut) Arial, 10 pt, Anglais (États-Unis)

Mis en forme : Police :(Par défaut) Arial, 10 pt, Anglais (États-Unis)

Mis en forme : Police :(Par défaut) Arial, 10 pt, Anglais (États-Unis)

Mis en forme : Police :(Par défaut) Arial, 10 pt, Anglais (États-Unis)

1183 Sun, Y. L., Zhang, Q., Anastasio, C., and Sun, J.: Insights into secondary organic aerosol formed via
 1184 aqueous-phase reactions of phenolic compounds based on high resolution mass spectrometry,
 1185 *Atmos. Chem. Phys.*, 10, 4809–4822, <https://doi.org/10.5194/acp-10-4809-2010>, 2010.

1186 Tang, M., Huang, X., Lu, K., Ge, M., Li, Y., Cheng, P., Zhu, T., Ding, A., Zhang, Y., Gligorovski, S.,
 1187 Song, W., Ding, X., Bi, X., and Wang, X.: Heterogeneous reactions of mineral dust aerosol:
 1188 implications for tropospheric oxidation capacity, *Atmos. Chem. Phys.*, 17, 11727–11777,
 1189 <https://doi.org/10.5194/acp-17-11727-2017>, 2017.

1190 Tegen, I. and Fung, I.: Contribution to the atmospheric mineral aerosol load from land surface
 1191 modification, *J. Geophys. Res.*, 100, 18707, <https://doi.org/10.1029/95JD02051>, 1995.

1192 Trainic, M., Abo Riziq, A., Lavi, A., Flores, J. M., and Rudich, Y.: The optical, physical and chemical
 1193 properties of the products of glyoxal uptake on ammonium sulfate seed aerosols, *Atmos. Chem.*
 1194 *Phys.*, 11, 9697–9707, <https://doi.org/10.5194/acp-11-9697-2011>, 2011.

1195 Turpin, B. J. and Huntzicker, J. J.: Identification of secondary organic aerosol episodes and quantitation
 1196 of primary and secondary organic aerosol concentrations during SCAQS, *Atmos. Atmospheric*
 1197 *Environment*, 29, 3527–3544, [https://doi.org/10.1016/1352-2310\(94\)00276-Q](https://doi.org/10.1016/1352-2310(94)00276-Q), 1995.

1198 Usher, C. R., Michel, A. E., and Grassian, V. H.: Reactions on Mineral Dust, *Chem. Rev.*, 103, 4883–
 1199 4940, <https://doi.org/10.1021/cr020657y>, 2003.

1200 Volkamer, R., Platt, U., and Wirtz, K.: Primary and Secondary Glyoxal Formation from Aromatics:
 1201 Experimental Evidence for the Bicycloalkyl–Radical Pathway from Benzene, Toluene, and p -
 1202 Xylene, *J. Phys. Chem. A*, 105, 7865–7874, <https://doi.org/10.1021/jp010152w>, 2001.

1203 Volkamer, R., Spietz, P., Burrows, J., and Platt, U.: High-resolution absorption cross-section of glyoxal
 1204 in the UV–vis and IR spectral ranges, *Journal of Photochemistry and Photobiology-Photobio. A:*
 1205 *Chemistry*, 172, 35–46, <https://doi.org/10.1016/j.jphotochem.2004.11.011>, 2005.

1206 Volkamer, R., San Martini, F., Molina, L. T., Salcedo, D., Jimenez, J. L., and Molina, M. J.: A missing
 1207 sink for gas-phase glyoxal in Mexico City: Formation of secondary organic aerosol, *Geophysical*
 1208 *Geophys. Research Res. Letters*, 34, 2007GL030752,
 1209 <https://doi.org/10.1029/2007GL030752>, 2007.

1210 Vrekoussis, M., Wittrock, F., Richter, A., and Burrows, J. P.: Temporal and spatial variability of glyoxal
 1211 as observed from space, *Atmos. Chem. Phys.*, 9, 4485–4504, [https://doi.org/10.5194/acp-9-](https://doi.org/10.5194/acp-9-4485-2009)
 1212 4485-2009, 2009.

1213 Vrekoussis, M., Wittrock, F., Richter, A., Burrows, J. P., and Cho, C.: Temporal and spatial variability of
 1214 glyoxal as observed from space, *Atmos. Chem. Phys.*, 2009.

1215 Wagner, C., Hanisch, F., Holmes, N., de Coninck, H., Schuster, G., and Crowley, J. N.: The interaction
 1216 of N₂O₅ with mineral dust: aerosol flow tube and Knudsen reactor studies, *Atmos. Chem. Phys.*,
 1217 8, 91–109, <https://doi.org/10.5194/acp-8-91-2008>, 2008.

1218 Wagner, C., Hanisch, F., Holmes, N., de Coninck, H., Schuster, G., and Crowley, J. N.: The interaction
 1219 of N₂O₅ with mineral dust: aerosol flow tube and Knudsen reactor studies, *Atmos. Chem. Phys.*,
 1220 2008.

1221 Walker, H., Stone, D., Ingham, T., Hackenberg, S., Cryer, D., Punjabi, S., Read, K., Lee, J., Whalley,
 1222 L., Spracklen, D. V., Carpenter, L. J., Arnold, S. R., and Heard, D. E.: Observations and modelling
 1223 of glyoxal in the tropical Atlantic marine boundary layer, *Atmos. Chem. Phys.*, 22, 5535–5557,
 1224 <https://doi.org/10.5194/acp-22-5535-2022>, 2022.

1225 Wang, G., Cheng, C., Meng, J., Huang, Y., Li, J., and Ren, Y.: Field observation on secondary organic
 1226 aerosols during Asian dust storm periods: Formation mechanism of oxalic acid and related
 1227 compounds on dust surface, *Atmospheric Environment*, 113, 169–176,
 1228 <https://doi.org/10.1016/j.atmosenv.2015.05.013>, 2015.

1229 Wang, J., Doussin, J. F., Perrier, S., Perraudin, E., Katrib, Y., Pangui, E., and Picquet-Varraut, B.:
 1230 Design of a new multi-phase experimental simulation chamber for atmospheric photosmog,
 1231 aerosol and cloud chemistry research, *Atmos. Meas. Tech.*, 4, 2465–2494,
 1232 <https://doi.org/10.5194/amt-4-2465-2011>, 2011.

Mis en forme : Indice

Mis en forme : Indice

- 1233 Washenfelter, R. A., Young, C. J., Brown, S. S., Angevine, W. M., Atlas, E. L., Blake, D. R., Bon, D. M.,
 1234 Cubison, M. J., De Gouw, J. A., Dusanter, S., Flynn, J., Gilman, J. B., Graus, M., Griffith, S.,
 1235 Grossberg, N., Hayes, P. L., Jimenez, J. L., Kuster, W. C., Lefer, B. L., Pollack, I. B., Ryerson, T.
 1236 B., Stark, H., Stevens, P. S., and Trainer, M. K.: The glyoxal budget and its contribution to organic
 1237 aerosol for Los Angeles, California, during CalNex 2010: ~~GLYOXAL-Glyoxal Budget BUDGET~~
 1238 ~~FOR~~ ~~Lfor~~ ~~LosOS~~ ~~AngelesNGELES~~, J. Geophys. Res., 116,
 1239 <https://doi.org/10.1029/2011JD016314>, 2011.
- 1240 Webb, N. P. and Pierre, C.: Quantifying Anthropogenic Dust Emissions, *Earth's Future*, 6, 286–295,
 1241 <https://doi.org/10.1002/2017EF000766>, 2018.
- 1242 Xu, K., Liu, Y., Li, C., Zhang, C., Liu, X., Li, Q., Xiong, M., Zhang, Y., Yin, S., and Ding, Y.: Enhanced
 1243 secondary organic aerosol formation during dust episodes by photochemical reactions in the
 1244 winter in Wuhan, ~~Journal of Environmental Environ. SciencesSci~~, 133, 70–82,
 1245 <https://doi.org/10.1016/j.jes.2022.04.018>, 2023.
- 1246 Zeineddine, M. N., Romanias, M. N., Gaudion, V., Riffault, V., and Thévenet, F.: Heterogeneous
 1247 Interaction of Isoprene with Natural Gobi Dust, *ACS Earth Space Chem.*, 1, 236–243,
 1248 <https://doi.org/10.1021/acsearthspacechem.7b00050>, 2017.
- 1249 Zeineddine, M. N., Urupina, D., Romanias, M. N., Riffault, V., and Thevenet, F.: Uptake and reactivity
 1250 of acetic acid on Gobi dust and mineral surrogates: A source of oxygenated volatile organic
 1251 compounds in the atmosphere?, ~~Atmospheric-Atmos. EnvironmentEnviron.~~, 294, 119509,
 1252 <https://doi.org/10.1016/j.atmosenv.2022.119509>, 2023.
- 1253 Zhang, X., He, A., Guo, R., Zhao, Y., Yang, L., Morita, S., Xu, Y., Noda, I., and Ozaki, Y.: A new approach
 1254 to removing interference of moisture from FTIR spectrum, *Spectrochimica Acta Part A: Molecular*
 1255 *and Biomolecular Spectroscopy*, 265, 120373, <https://doi.org/10.1016/j.saa.2021.120373>, 2022.
- 1256 Zhang, Y., He, L., Sun, X., Ventura, O. N., & Hermann, H. (2022). Theoretical Investigation on the
 1257 Oligomerization of Methylglyoxal and Glyoxal in Aqueous Atmospheric Aerosol Particles. *ACS*
 1258 *Earth and Space Chemistry*, 6(4), 1031–1043.
 1259 <https://doi.org/10.1021/acsearthspacechem.1c00422>
- 1260 Zielinski, A. T., Kourtchev, I., Bortolini, C., Fuller, S. J., Giorio, C., Popoola, O. A. M., Bogialli, S.,
 1261 Tapparo, A., Jones, R. L., and Kalberer, M.: A new processing scheme for ultra-high resolution
 1262 direct infusion mass spectrometry data, ~~Atmos. Environ. Atmospheric Environment~~, 178, 129–
 1263 139, <https://doi.org/10.1016/j.atmosenv.2018.01.034>, 2018.